

Original Article

Cite this article: Wang ZL, Tranos MD, Wang X, Zhao RX, and Zhang RF (2023) ^{40}Ar – ^{39}Ar geochronology and palaeostress analysis using lamprophyre dikes and quartz veins in the Sizhuang gold deposit: new implications for Early Cretaceous stress regime in the Jiaodong Peninsula, North China Craton. *Geological Magazine* **160**: 623–644. <https://doi.org/10.1017/S0016756822001029>

Received: 18 April 2022

Revised: 3 September 2022

Accepted: 4 September 2022

First published online: 21 October 2022

Keywords:



dikes and veins; phlogopite ^{40}Ar – ^{39}Ar dating; palaeostress reconstruction; transtension; East Asia

Author for correspondence:

Zhongliang Wang,

Email: zhong.liangw@163.com

^{40}Ar – ^{39}Ar geochronology and palaeostress analysis using lamprophyre dikes and quartz veins in the Sizhuang gold deposit: new implications for Early Cretaceous stress regime in the Jiaodong Peninsula, North China Craton

Zhongliang Wang¹ , Markos D Tranos² , Xuan Wang¹, Rongxin Zhao³ and Rifeng Zhang¹

¹School of Earth Sciences and Resources, China University of Geosciences, Beijing 100083, China; ²Department of Structural, Historical & Applied Geology, Aristotle University of Thessaloniki, Thessaloniki 54124, Greece and ³Jiaojia Gold Company, Shandong gold mining stock co., LTD, Laizhou city, Shandong province 261438, China

Abstract

Lamprophyre dikes and quartz veins in the Sizhuang gold deposit are used to date and unravel the Early Cretaceous stress regime in the Jiaodong Peninsula, North China Craton. The lamprophyre dikes are grouped into two major sets, trending NNW–SSE and NNE–SSW, respectively, and a subsidiary one, trending WNW–ESE, whereas the quartz veins trend mainly NNE–SSW. The age of lamprophyre dikes' intrusion was robustly calculated at c. 119 Ma by phlogopite ^{40}Ar – ^{39}Ar dating. The fuzzy clustering technique defined four stress states, which were grouped into three stress regimes in Sizhuang. Furthermore, these stress regimes were interrelated with two regional far-field stress regimes, ST1 and ST2, defined by the available published fault-slip data near Sizhuang by applying the separation and stress inversion TR method (TRM). The palaeostress reconstruction indicates that extension and strike-slip tectonics (i.e. transtension) affect the emplacement of the lamprophyre dikes and quartz veins. More precisely, the dike emplacement occurred under unstable stress conditions related to the shift from E–W pure extension–transtension to WNW–ESE transtension, whereas the quartz veins formed under relatively stable WNW–ESE transtension with the variant and increasing fluid pressure (P_f) giving rise to the strike-slip against dip-slip kinematics along the faults. The change from the ST1 to ST2 stress regimes reflects the significant clockwise rotation in the palaeo-Pacific plate subduction direction and defines the switching time at c. 119 Ma as precisely obtained by the lamprophyre dating.

1. Introduction

The North China Craton (NCC), resulting from the cratonization in the Palaeoproterozoic (c. 1.85 Ga) (Zhao *et al.* 2005), occupies a large part of East Asia towards the Pacific Ocean (Fig. 1a). The NCC acted as a stable block until the late Palaeozoic (Zhao *et al.* 2005; Santosh *et al.* 2007). It had been tectonically reactivated due to the collision to the north with the Palaeozoic Mongolian arcs during the Late Permian (Xiao *et al.* 2003), and to the south with the Yangtze Craton (YC) in the Middle–Late Triassic (Dong *et al.* 2011). The latter orogenesis led to the amalgamation of the Sulu terrane in the southeast with the Jiaobei terrane in the northwest via the lithospheric-scale ENE–WSW- to NE–SW-trending Wulian–Qingdao–Yantai Fault (WQYF), forming the Jiaodong Peninsula on the East Asian margin (Fig. 1a, b) (Guo *et al.* 2013). It has been widely accepted that the subsequent tectonic evolution of the Jiaodong Peninsula was intimately related to the palaeo-Pacific subduction (Ratschbacher *et al.* 2000; Sun *et al.* 2007). The convergent processes resulted in the de-cratonization and lithospheric thinning in the eastern NCC from the Late Jurassic to Early Cretaceous (Zhu *et al.* 2010), as well as the widely developed gold mineralization in the Jiaodong Peninsula during the Early Cretaceous (Wang *et al.* 2015). The palaeo-Pacific plate subducted towards East Asia at varying speeds and angles since the Mesozoic (Liu *et al.* 2017), and there were significant changes in subduction direction in the Early Cretaceous from the WNW during 139–122 Ma to the NW during 121–95 Ma (Sager, 2006; Zhu & Xu, 2019). Nevertheless, the Early Cretaceous palaeostresses driving the gold deposits in the Jiaodong Peninsula (Fig. 1a, b), one of the major gold provinces globally and the leading gold producer in China (Zhu *et al.* 2015), are still under debate.

Previous geochemical and geochronological studies on magmatic activities, large-scale gold mineralization and the formations of the volcanic–sedimentary basins in the Jiaodong Peninsula led to strong controversies on the Early Cretaceous palaeostresses (Zhu *et al.* 2005;

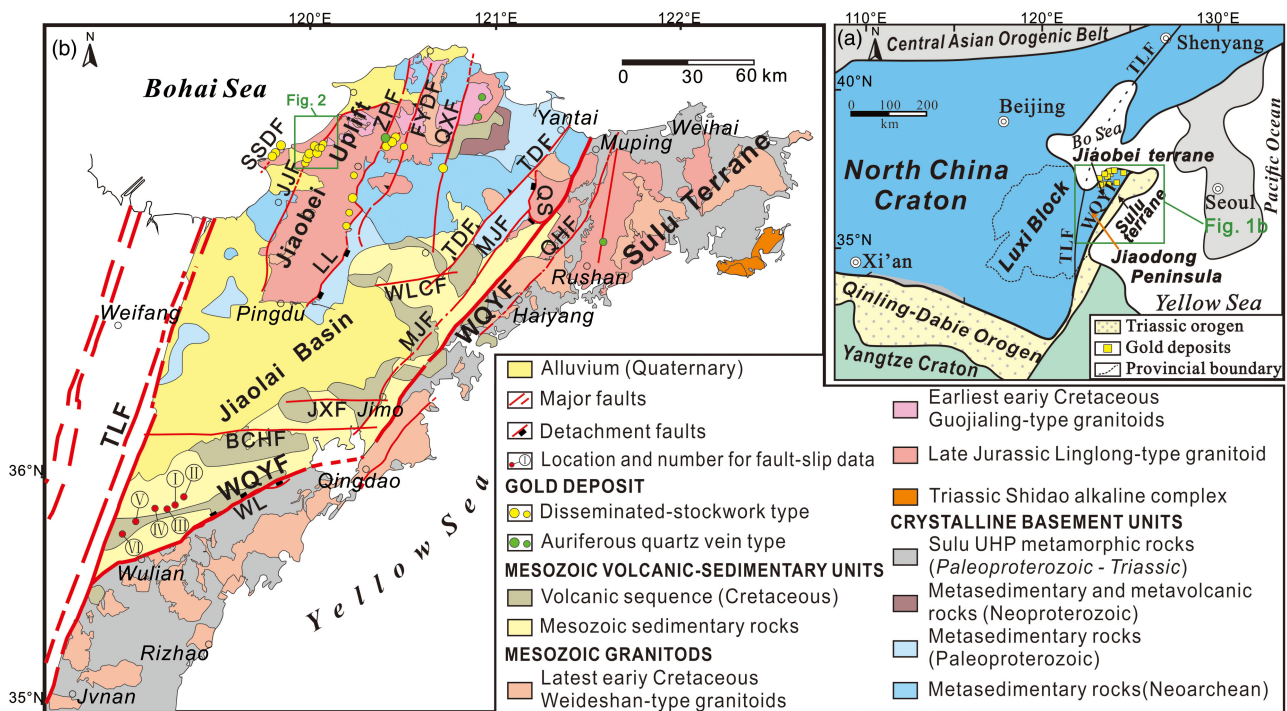


Fig. 1. (Colour online) (a) A simplified tectonic map of the North China craton showing the location of the Jiaodong Peninsula, the distribution of late Mesozoic intrusions, and major districts hosting large gold deposits in the eastern half of the craton (modified from Li *et al.* 2012). (b) A simplified geological map of the Jiaodong Peninsula showing the distribution of Precambrian crystalline basement, Triassic UHP metamorphic rocks, Cretaceous volcanic-sedimentary sequence, Mesozoic granitoids, major structures, and representative gold deposits (modified from Wang *et al.* 2015). The locations for fault-slip data are from B Zhang *et al.* (2020). Main faults: WQYF, Wulian-Qingdao-Yantai Fault; TLF, Tan-Lu Fault; ZPF, Zhaoping Fault; SSDF, Sanshandao Fault; JJF, Jiaojia Fault; FYDF, Fengyidian Fault; QXF, QiXia Fault; TDF, Taocun-Dongdoushan Fault; MJF, Muping-Jimo Fault; QHF, Qingdao-Haiyang Fault; MRF, Muping-Rushan Fault; WLCF, Wulongcun Fault; JXF, Jiuxian Fault; BCHF, Baichihe Fault. Metamorphic Core Complex (MCC): LL, Linglong MCC; WL, Wulian MCC; QS, Queshan MCC. Fault-slip data: I, K1Ly-05; II, K1Ly-06; III, K1Ly-07; IV, K1Ly-10; V, K1Ly-25; VI, K1Ly-27.

Sun *et al.* 2007; Wang *et al.* 2019). The tectonic regime in the Jiaodong Peninsula during the Early Cretaceous has been suggested to be (a) changing from extension (140–125 Ma) through transpression (125–120 Ma) to extension (120–100 Ma) (Zhu *et al.* 2005; Sun *et al.* 2007), (b) changing from extension (140–122 Ma) through transpression (122–111 Ma) to extension (110–100 Ma) (Wang *et al.* 2016, 2019) or (c) changing from compression to extension at *c.* 120 Ma (KF Yang *et al.* 2018). On the other hand, fault-slip analyses in the Jiaolai Basin (Fig. 1b) (YQ Zhang *et al.* 2003, 2008; Ren *et al.* 2007; B Zhang *et al.* 2020) suggest an extensional tectonic regime only, with the extensional direction showing rotation in the Jiaodong Peninsula during the Early Cretaceous. However, both the model and the timing of the rotation of extensional direction remain controversial, including from N–S to WNW–ESE at 120 Ma (Zhang *et al.* 2003), from NW–SE to WNW–ESE at 115 Ma (Ren *et al.* 2007), from NW–SE to WNW–ESE at 120 Ma (Zhang *et al.* 2008) and from E–W to NW–SE at 120 Ma (B Zhang *et al.* 2020). These controversies may be due to multiple deformation events experienced by these faults (Zhang *et al.* 2007), the complex chronostratigraphic sequence and the inaccurate strata dating in the Jiaolai Basin (B Zhang *et al.* 2020).

Lamprophyre dikes and hydrothermal quartz veins, usually showing tabular geometric features, provide vital information on the palaeostresses under which they formed (Mazzarini & Musumeci, 2008; Skarmeta, 2011; Martinez-Poza & Druguet, 2016). In particular, they have been considered to be normal to the regional least principal compressive stress (σ_3) direction (Babiker & Gudmundsson, 2004). Thus, the orientations of lamprophyre dikes or quartz veins can be directly used to infer

the directions of palaeostresses (Gudmundsson & Marinoni, 2002). However, the shapes of dikes and veins are usually strongly affected by the mechanical properties of their host rocks. They seldom dilate a single fracture in most cases, whereas they are often arranged on arrays of sub-parallel segments and fingers with shapes that depend on the host-rock lithology, stress field and pre-existing fractures (Pollard *et al.* 1975; Baer, 1991). In general, dikes and veins propagate along the older fractures not necessarily normal to the σ_3 direction (Delaney *et al.* 1986; Khodayar & Einarsson, 2002), which results in their attitude variations (Sato *et al.* 2013). Therefore, in these instances, lamprophyre dikes and quartz veins do not pertain to a simple relation to the regional stress field (Mazzarini & Musumeci, 2008; Creixell *et al.* 2011). Fortunately, the variations in the orientations of the dikes and veins carry clues to the parameters of stress tensors (Baer *et al.* 1994; Sato *et al.* 2013), and the development of palaeostress inversion techniques for dilatant fractures, such as dikes and veins, has made it possible to determine three-dimensional palaeostress conditions by analysis of their attitude variations (Baer *et al.* 1994; Jolly & Sanderson, 1997; Yamaji & Sato, 2011; Yamaji, 2016; Faye *et al.* 2018). These techniques are based on the mechanical fundamental that whether the fracture reopens or not is controlled by the equilibrium of the normal stress (σ_n) and the fluid pressure (P_f) imposed on it (Anderson, 1939; Delaney *et al.* 1986; Pollard, 1987). Nevertheless, the magnitude of σ_n rests with the fracture orientation, which results in the dilatant fractures showing the anisotropic orientation distribution (Sato *et al.* 2013). Accordingly, using these techniques, the directions of the three principal stress axes σ_1 , σ_2 and σ_3 , with $\sigma_1 \geq \sigma_2 \geq \sigma_3$ of the stress ellipsoid, and its stress ratio $\Phi = (\sigma_2 - \sigma_3) / (\sigma_1 - \sigma_3)$ with $1 \geq \Phi \geq 0$, i.e. the ratio of the relative

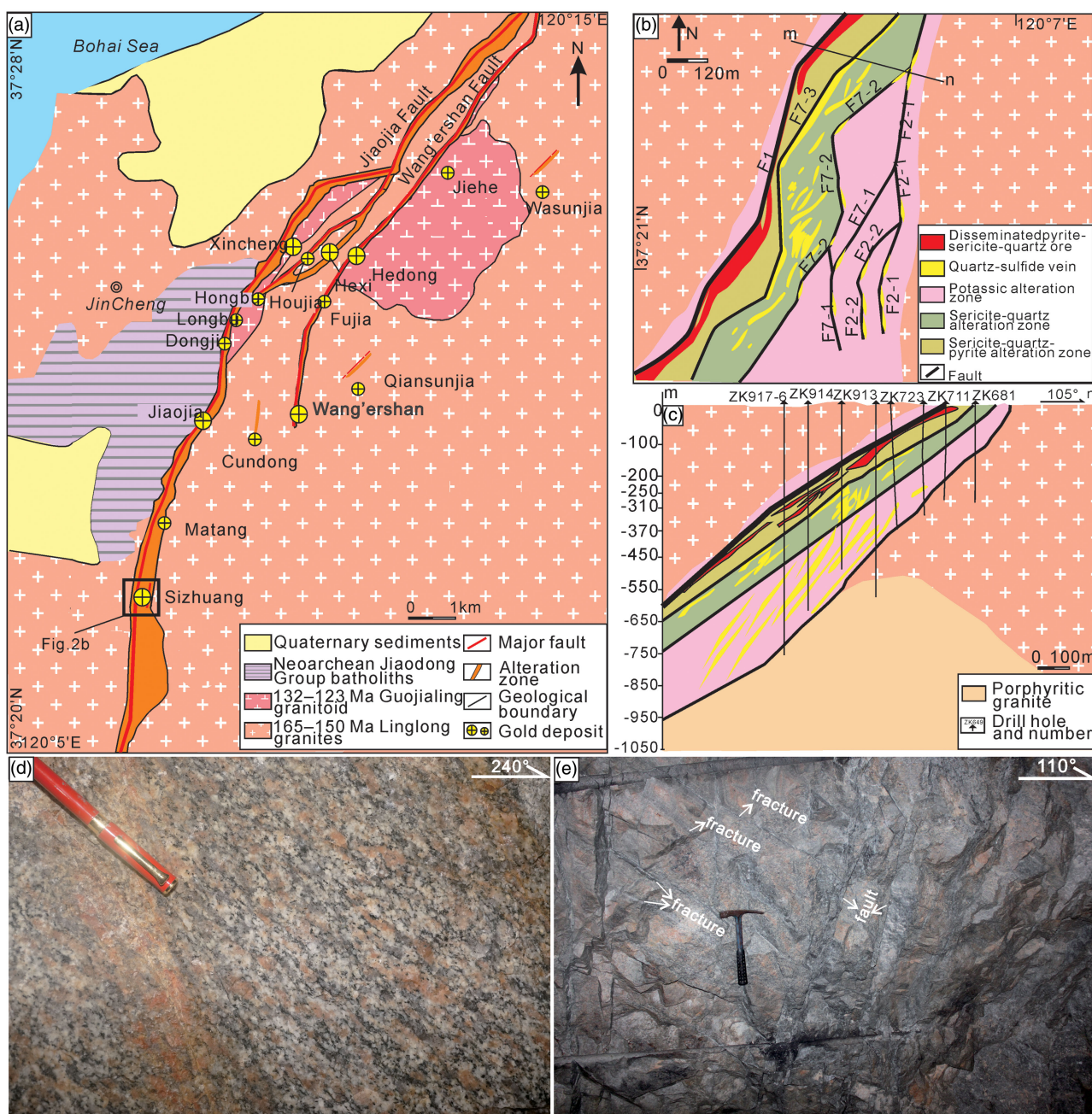


Fig. 2. (Colour online) (a) A simplified geological map of the Jiaojia gold camp showing the distribution of ore-controlling structures and representative gold deposits (modified from Wang *et al.* 2015). Differently sized symbols of gold deposits show different gold resources: the larger symbols shows Au > 50 t, and the smaller symbols show Au < 50 t. The Sizhuang gold deposit is situated in the southern part of the Jiaojia Fault. (b) Geologic map and (c) typical cross-section of the ore body and fault zone in the Sizhuang gold deposit, showing the structural controls on hydrothermal alteration and mineralization. (d) Field view of the gneissic foliation in the fresh Linglong granite. (e) Field view of faults and fractures affecting the K-feldspar altered granite.

magnitudes of the principal stresses (Bishop, 1966; Angelier, 1975), as well as the driving pressure ratio $R' = (P_f - \sigma_3) / (\sigma_1 - \sigma_3)$, which defines the magnitude of the fluid pressure (P_f) in relation to the maximum and minimum principal stresses (Baer *et al.* 1994), can be defined (Jolly & Sanderson, 1997; Martínez-Poza *et al.* 2014; Faye *et al.* 2018). Thus, the stress regime related to the emplacement of the dikes and veins can be inferred (André *et al.* 2001; Mondal & Mamtani, 2013; Goswami *et al.* 2021). Therefore, undeformed dikes and veins are among the most important structural elements applied for palaeostress analysis (Pollard, 1987; Mazzarini *et al.* 2010; Jaques & Pascal, 2017; Lahiri *et al.* 2020).

Lamprophyre dikes and hydrothermal quartz veins were widely developed in the gold deposits in the Jiaodong Peninsula (Wang *et al.* 2015; Li *et al.* 2016). Due to the limited outcrops, we could not perform the systematic geological survey on the dikes and quartz veins on the surface. However, the 22 levels of block caving between -40 m and -870 m elevation in the Sizhuang gold mine, located at the southern extremity of the Jiaojia gold camp in north-west Jiaodong Peninsula (Figs 1a and 2), have revealed the lamprophyre dikes and quartz veins underground systematically. The excellent underground exposures of lamprophyre dikes and quartz veins in the Sizhuang mine allow us to comprehensively investigate

their geometric properties and attitudes along-strike and -dip in this study. This paper first reports the structural patterns of the lamprophyre dikes and quartz veins in the Sizhuang gold deposit, then employs the fuzzy clustering technique of Yamaji and Sato (2011) to infer the three-dimensional (3D) palaeostress state and the driving fluid pressure during the formation of the lamprophyre dikes and quartz veins. In addition, given that no information on the emplacement age of the lamprophyre dikes in Sizhuang has been published, we performed the ^{40}Ar – ^{39}Ar dating on the phlogopites selected from the lamprophyre dikes to constrain the time of structural deformation when the dikes were formed.

The present work obtains the timing and the palaeostress states during the emplacement of the lamprophyre dikes and quartz veins in the Sizhuang gold deposit and further sheds new light on the Early Cretaceous stress regime in the Jiaodong Peninsula.

2. Geological setting

The Jiaodong Peninsula, located at the southeastern margin of NCC, consists of the Sulu terrane in the southeast and the Jiaobei terrane in the northwest (Fig. 1a). The two terranes are separated by the lithospheric-scale ENE- to NE-trending Wulian–Qingdao–Yantai Fault (WQYF; Fig. 1a, b). The Jiaodong Peninsula is bounded by the Pacific Plate to the east and separated from the Luxi Block of the NCC by the 2400 km long NNE–SSW- (between 010° and 025°) trending and steeply dipping Tan-Lu Fault (TLF) to the west (Yan *et al.* 2014). The striking feature of the peninsula is the regional-scale NNE–SSW- to NE–SW-striking faults, which were developed either in the cratonic interior or along pre-existing suture zones like the TLF, Zhaoyuan–Pingdu Fault (ZPF) and WQYF, respectively, from west to east (Fig. 1b; Liu *et al.* 2021).

The basement in the Sulu terrane, to the southeast of the WQYF, is composed of Palaeoproterozoic and Neoproterozoic crystalline rocks of YC (Li *et al.* 1993) and was subjected to an ultrahigh-pressure (UHP) metamorphic event at *c.* 244–220 Ma (Cong, 1996). The Jiaobei terrane to the northwest of the WQYF (Faure *et al.* 2001) includes the Jiaobei Uplift and the Jiaolai Basin (Fig. 1b; Wang *et al.* 2014). The Jiaobei Uplift is mainly composed of the Precambrian high-grade metamorphic rocks of NCC (Fig. 1b; Tang *et al.* 2007). The latter rocks were intruded by the Linglong granite between 163 and 149 Ma (Yang *et al.* 2012), which subsequently uplifted between *c.* 143 and 128 Ma during the exhumation of the Linglong metamorphic core complex (Charles *et al.* 2013) and the contemporaneous formation of the Jiaolai Basin (Liu *et al.* 2021). The Jiaolai Basin consists of the clastic and volcanic rocks that span the period from 135 Ma (Ni *et al.* 2016) to 55 Ma and is grouped into the Laiyang, Qingshan, Dasheng, Wangshi and Wutu Groups from bottom to top (B Zhang *et al.* 2020). Except for the limited occurrence of 215–200 Ma Shidao alkaline complex occurring in the southeastern boundary of the Sulu terrane (Yang *et al.* 2005), the widely developed magmatism both in the Jiaobei Uplift and the Sulu terrane occurred during the Late Jurassic – Early Cretaceous (Fig. 1b; Wang *et al.* 2014). The Late Jurassic Linglong-type granitoids usually exhibit a NNE–SSW-trending mylonitic foliation associated with the WNW–ESE-trending stretching lineations (LQ Yang *et al.* 2018). In contrast, the Early Cretaceous granitic plutons are undeformed (QY Yang *et al.* 2014).

The emplacement of the Late Jurassic Linglong-type granitoids, with the magmas produced by the partial melting of the juvenile crust with the alkaline rocks of the Sulu terrane and the lower crust containing the garnet–amphibolite of the Jiaobei terrane

(Hou *et al.* 2007), was induced by the rapid and steepening rollback of the Palaeo-Pacific plate during 165–160 Ma (LQ Yang *et al.* 2018). The latter symbolized the initiation of a lithospheric tectonic extension and the associated magmatism in the Jiaodong Peninsula, which continued into the Early Cretaceous time (Liu *et al.* 2015). Accordingly, in the Early Cretaceous time (135–110 Ma), the crustal deformation in the Jiaodong Peninsula was dominated by various extensional structures, such as extensional basins, normal faults, low-angle detachment faults and metamorphic core complexes (MCCs) (Fig. 1; Liu *et al.* 2021), accompanied by extensive gold mineralization (Fig. 1; Goldfarb *et al.* 2014).

The Precambrian basement rocks in the Jiaobei terrane display a gross E–W-trending tectonic fabric at a regional scale prior to the emplacement of the Late Jurassic Linglong-type granitoids, which is associated with the broadly E–W-trending reverse faults and ENE–WSW- to E–W-trending shear zones in the Archaean and Palaeoproterozoic rocks (Lu *et al.* 2007). By contrast, the Mesozoic magmatic rocks, the MCCs, the Jiaolai Basin and the crustal- to lithospheric-scale oblique-slip faults showing both transpressional and transtensional kinematics, i.e. TLF and WQYF (Meng, 2003; Wang *et al.* 2011), collectively exhibit strong NE–SW- to NNE–SSW-aligned tectonic fabric (Fig. 1b; LQ Yang *et al.* 2018).

The TLF developed as a Late Jurassic left-lateral strike-slip fault and then reactivated as a normal fault in the Early Cretaceous, controlling the development of the Jiaolai Basin (Fig. 1; Zhu *et al.* 2010). However, more recently, B Zhang *et al.* (2020) argued that the TLF initially occurred as a normal fault under a NW–SE extension from *c.* 120 to 93 Ma, postdating the deposition of the Laiyang Group under the E–W extension between *c.* 135 and 122 Ma. The E–W extension led to the activity of the WQYF along the suture zone connecting the Jiaobei and Sulu terranes (B Zhang *et al.* 2020). The WQYF, striking ENE–WSW to NE–SW and dipping at gentle to medium angles to the NNW to NW (B Zhang *et al.* 2020), is considered to occur in the upper-middle crust from *c.* 135 to 122 Ma, causing the initial expansion of the Jiaolai Basin, then progressing into the lithospheric mantle from *c.* 122 to 110 Ma (Liu *et al.* 2021). Many lower-order faults, striking NNE–SSW to NE–SW, were developed within the Jiaobei Uplift and the Sulu terrane. On the other hand, only a few nearly E–W normal faults occurred within the Jiaolai Basin (Fig. 1b). The NNE- to NE-trending faults with dips either to the NW or SE are distributed across the Jiaobei Uplift and the Sulu terrane, with an interval of *c.* 15–35 km, on both sides of the ZPF and WQYF (Fig. 1b), which are named as the Sanshandao, Jiaojia, Fengyidian, Qixia, Taocun–Dongdoushan, Muping–Jimo, Qingdao–Haiyang and Muping–Rushan faults from west to east (Fig. 1b), respectively.

The Jiaojia Fault, striking NNE–SSW (between 010° and 030°) and dipping WNW with angles of 20 – 40° , controls the Sizhuang gold deposit (Fig. 2a). The mine is established on the Linglong granite (Fig. 2b), which was replete with many irregular and discontinuous lamprophyre dikes, and a great number of quartz veins (Wei *et al.* 2019; Fig. 2c). The host granite is dominated by a gneissic foliation better seen in the fresh exposures (Fig. 2d) that generally trends NNE–SSW to NE–SW (Wang *et al.* 2015), and the faults and fractures better seen in the altered parts of the granite (Fig. 2e). Three alteration zones are identified in the footwall of the Jiaojia Fault, going from the unaltered granite to the Jiaojia Fault plane (Fig. 2b): (a) the potassic, (b) the sericite–quartz and (c) the pyrite–sericite–quartz alteration zone. The pyrite–sericite–quartz alteration zone was characterized by a network of multi-directional quartz–sulphide veinlets, typically 0.2 to 1 cm thick (Fig. 2b). In the sericite–quartz and potassic



Fig. 3. (Colour online) Field photographs of the lamprophyre dikes in the Sizhuang gold deposit. (a) WNW-striking steep-dipping lamprophyre dike, with sharp straight contacts and (b) NNW-SSE-striking continuous dike segments, with non-overlapping and zigzag morphologies, in the K-feldspar altered granites. (c) NNE-SSW-striking dike segments with non-overlapping morphologies and horns beyond the offset step. (d) NNE-SSW-striking dike with small stepping continuous offsets in the K-feldspar altered granites. Note the localized dike-normal quartz veins near the stepovers in (c) and (d). (e) NNW-striking continuous dike segments with small stepping offset and horn beyond the offset step in the sericite-quartz altered granites. Note the quartz vein cutting through the step segment sharply. (f) NNE-SSW-striking discontinuous dike segments with lower-stepping overlapping offsets in the K-feldspar altered granites. Note the dike-normal quartz veins restricted to rock-bridge zone. (g) NNE-striking discontinuous dike segments with upper-stepping non-overlapping offsets in the sericite-quartz altered granites. Note the slight curvatures around dike tips. (h) NW-SE-striking discontinuous dike segments with lower-stepping non-overlapping offsets in the sericite-quartz altered granites. Note the slight curvature in the internal part and the thin apophyse in the outer part around dike tips.

alteration zones, the veins are mainly single quartz-sulphide veins varying from 1 to 500 cm in thickness, controlled by the brittle fracture networks (Fig. 2b).

3. Lamprophyre dikes and quartz veins of the Sizhuang gold deposit: occurrence, sampling and acquisition

Lamprophyre dikes are abundant and cut across the Linglong granite in the Sizhuang mine with lengths of several tens of metres

to more than 100 m. Most dikes occur within the altered granites, are sub-vertical and, as a rule, have variable strike orientations such as WNW-ESE (Fig. 3a), NNW-SSE (Fig. 3b, e), NNE-SSW (Fig. 3c, d, f, g) and NW-SE (Fig. 3h), although only a few dikes are inclined (Fig. 3c, d). Their thicknesses vary from 8 to 90 cm. As observed in the underground Sizhuang gold mine, the lamprophyre dikes show sharp contacts, with some chilled, against the host Linglong granite (Fig. 3a-h). Few dikes are straight with parallel edges in sub-vertical sections (Fig. 3a) because most dikes

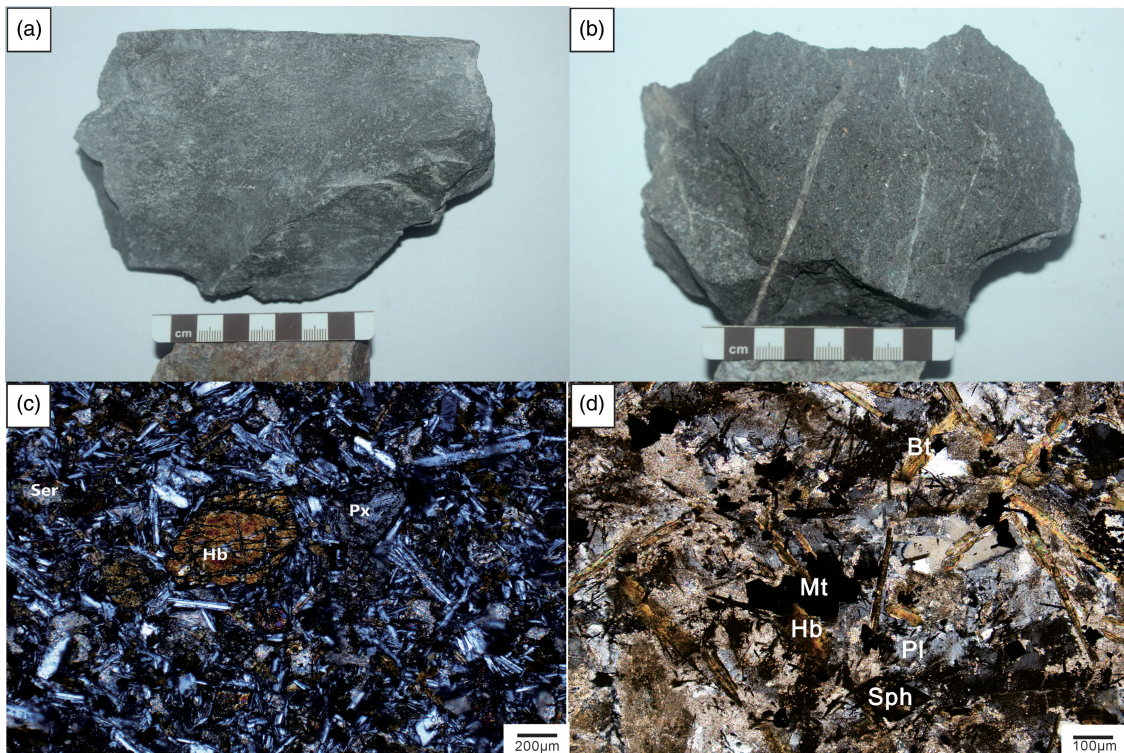


Fig. 4. (Colour online) Hand sample and micro-scale photographs of the lamprophyre dikes in the Sizhuang gold deposit. (a, b) Lamprophyre dike samples SZ16D004B1 and SZ16D002B2 for ^{40}Ar – ^{39}Ar dating. (c) Pyroxene and hornblende phenocrysts in an undeformed matrix of pyroxene, biotite, hornblende and plagioclase. (d) Biotite, hornblende and plagioclase, with accessory minerals of zircon, sphene and magnetite. Mineral abbreviations: Hb = hornblende, Px = pyroxene, Bt = biotite, Mt = magnetite, Pl = plagioclase, Sph = sphene, Ser = sericite.

are displaced, forming continuous (Fig. 3b–e) or discontinuous dike bodies (Fig. 3f–h) and zigzag (Fig. 3b) or sinuous shapes along their long dimensions (Fig. 3c–h). In some cases, displacements cause much more complicated dike patterns (Fig. 3b, c). Nevertheless, it seems that the dike bodies are aligned parallel to the pre-existing joints trending $\sim\text{N}0^\circ\text{--N}042^\circ$ (Fig. 3d) and $\sim\text{N}130^\circ\text{--N}175^\circ$ (Fig. 3b, e), showing that the magma propagation took place along the pre-existing joint sets (Fig. 3d, e).

The fact that slickenlines have hardly been observed along the dike margins implies more dilational than shear intrusion origin. Discontinuous dikes are characterized by an en echelon array of long tabular bodies striking NNE–SSW ($\sim 0\text{--}042^\circ$; Fig. 3f, g) and NW–SE to NNW–SSE ($\sim 130\text{--}175^\circ$; Fig. 3h), respectively. They form upwards-, left- or right-stepping geometries (Fig. 3f) with or without overlapping (Fig. 3g, h). Dike tips are frequently bent, appearing as horn structures (Fig. 3f–h), whereas apophyses between two opposite-directed dike tips often occur (Fig. 3h). In addition, some quartz veins oriented at high angles or perpendicular to the dikes occur within the bridge zones formed by the $\sim\text{N}0^\circ\text{--N}042^\circ$ dikes (Fig. 3f) but not along the $\sim\text{N}130^\circ\text{--N}175^\circ$ dikes (Fig. 3h).

Based on the detailed field and structural observations, two representative fresh and non-deformed lamprophyre dike samples of SZ16D004B1 (Fig. 4a) and SZ16D002B2 (Fig. 4b) were picked from the underground adits in the Sizhuang gold deposit. The sample SZ16D004B1 (Fig. 4a) was collected from a lamprophyre dike cutting the K-feldspar altered granite with a dip to the NW at 60° ($300\text{--}60^\circ$) (Fig. 3d). The sample SZ16D002B2 (Fig. 4b) was collected from a lamprophyre dike dipping WNW at 70° ($290\text{--}70^\circ$), which cut the sericite–quartz altered granite (Fig. 3g). They are porphyritic to equigranular and consist of pyroxene,

biotite, phlogopite and hornblende phenocrysts in a microcrystalline matrix of pyroxene, biotite, phlogopite, hornblende and plagioclase accompanied by accessory minerals including sphene, magnetite and zircon (Fig. 4c, d). These samples are used for dating the lamprophyre dikes with the ^{40}Ar – ^{39}Ar analysis of the phlogopite.

In general, the quartz veins show rough surfaces without slickenlines and tapering geometries (Fig. 5a) and have quartz crystals (sub)perpendicular to the fracture wall (Fig. 5b), indicating the dilational origin. Their lengths are usually more than 1 m and can be up to 200 m, whereas their thicknesses vary between 2 mm and 5 m. The smaller veins with lengths up to 20 m usually form a mesh-like structure with mutually cross-cutting relationships (Fig. 5c). In contrast, the bigger veins usually occur, in (sub)parallel bands (Fig. 5d, e), although in a few cases one band intersects another (Fig. 5f). In addition, while most of them have planar shapes (Fig. 5a–f), some zigzag or curved alignments can be observed (Fig. 6a, b). The rough surfaces of the veins and the zigzag or curved alignments suggest the mode I or mixed-mode formation of the filled cracks. In addition, many veins are accompanied by offshoots, which depart either clockwise or anticlockwise from them (Fig. 6c, d).

The attitudes of the lamprophyre dikes and quartz veins in the underground shaft of the Sizhuang mine were collected in two perpendicular directions from drive to drive in the study area, i.e. parallel and perpendicular to the mean strike (015°) of the main ore body. Based on the data acquisition technique and principle of Yamaji *et al.* (2010) and Lahiri and Mamtani (2016), the threshold values of 0.5 cm and 1 m for the thickness and length, respectively, of a mining face are used in the present study. For the dikes and quartz veins, if they are planar and single, the orientations were

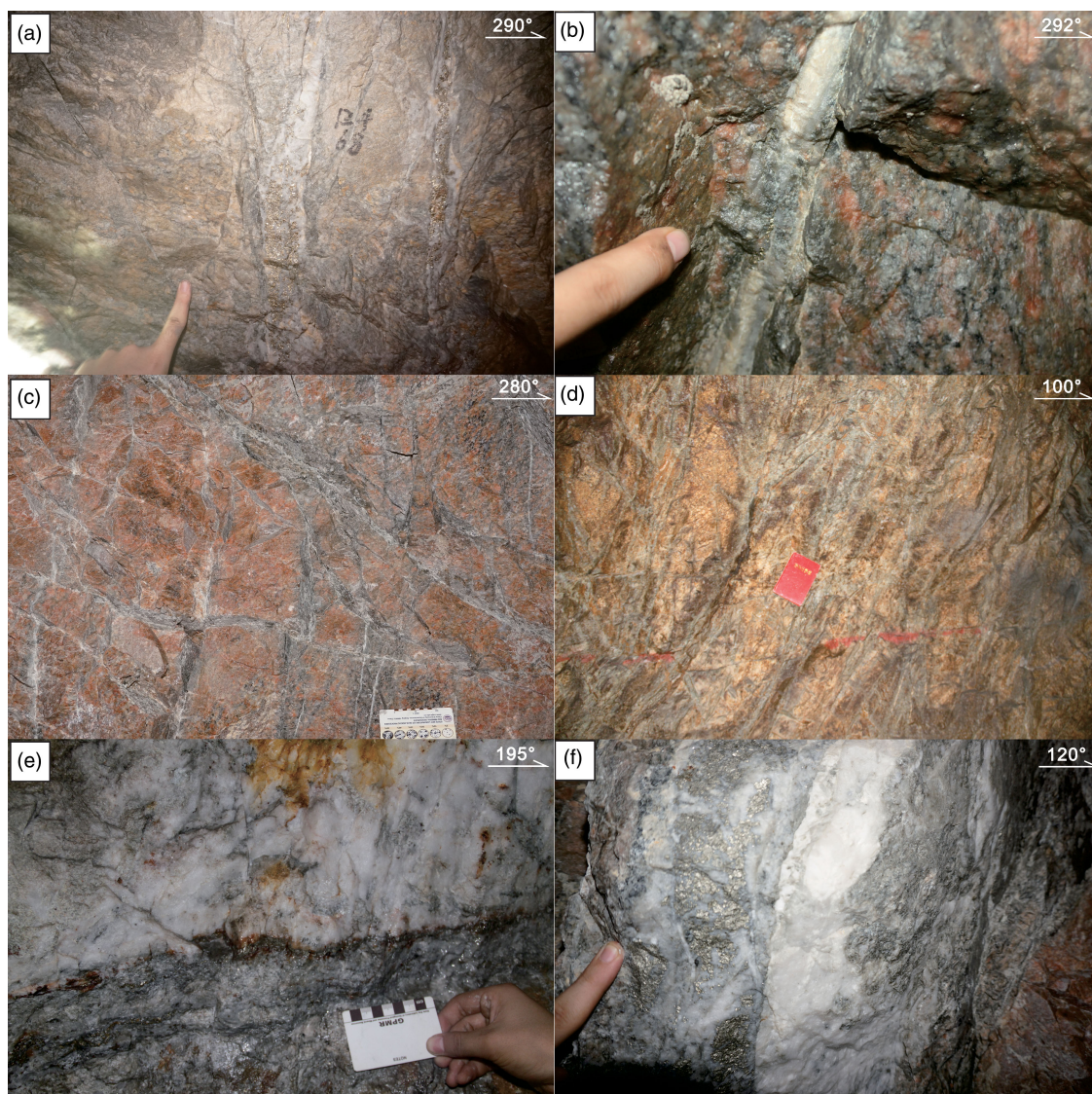


Fig. 5. (Colour online) Field photographs showing the occurrence of the quartz veins in the Sizhuang gold deposit. (a) Quartz vein with tapering geometry; (b) quartz veins with the quartz grains growing perpendicular to the fracture walls; (c) quartz veins showing a mesh-like structure with mutually cross-cutting relationships; (d) sub-parallel banded quartz veins; (e) banded quartz veins; (f) banded quartz veins including a few bands of different orientations.

measured when they fitted the above criteria; if they are planar and banded, each band meeting the criteria was measured. In the case of curved dikes and quartz veins, the attitude of each planar segment of those fitting the criteria was collected, whereas if they were longer than the threshold but had short-wavelength curves, we measured the average attitude.

Orientation data of 79 lamprophyre dikes and 320 quartz veins were collected in the underground shaft of the Sizhuang gold deposit. The lamprophyre dikes strike mainly NNW–SSE and NNE–SSW, whereas WNW–ESE is a subordinate direction (Fig. 7a, b). The NNW–SSE-striking set is the most populated, including the strikes from azimuths 310° to 355° , with an average azimuth at 338° (Fig. 7a). The NNE–SSW-striking set includes the strikes from azimuths 0° to 042° , with an average azimuth at 023° (Fig. 7a). The WNW–ESE-striking set only accounts for a small percentage of the very steep to almost vertical dikes striking from 275° to 295° (Fig. 7a, b). These dikes are shorter than those grouped into the two main sets (Fig. 3c–f). Moreover, the dikes dipping in

general to the W are well separated into two sets, but not the dikes dipping to the E (Fig. 7b).

Since a cross-cutting relationship between the two dike sets can hardly be concluded, we imagine the differently oriented dikes have intruded into the pre-existing fractures with geometries induced by the left-lateral strike-slip tectonics mentioned for the TLF during Late Jurassic times (Zhu *et al.* 2010). In particular, these fractures are (a) NNE–SSW-striking fractures dipping to the WNW parallel to the Jiaojia Fault, (b) NNW–SSE-striking Riedel shears dipping to the WSW, and (c) WNW–ESE-striking R' Riedel shears dipping to the SSW.

The quartz veins strike mainly NNE–SSW with azimuths from 0° to 45° and a mean azimuth at 017° dipping towards the WNW in their majority (>70%) (Fig. 7c, d). As a rule, they seem to have followed fractures parallel to the Jiaojia Fault.

It has been observed that the quartz veins cut sharply across the NNW–SSE- ($\sim 310^{\circ}$ – 355°) trending continuous dikes (Fig. 3e), showing that the NNW–SSE-trending lamprophyre dikes formed

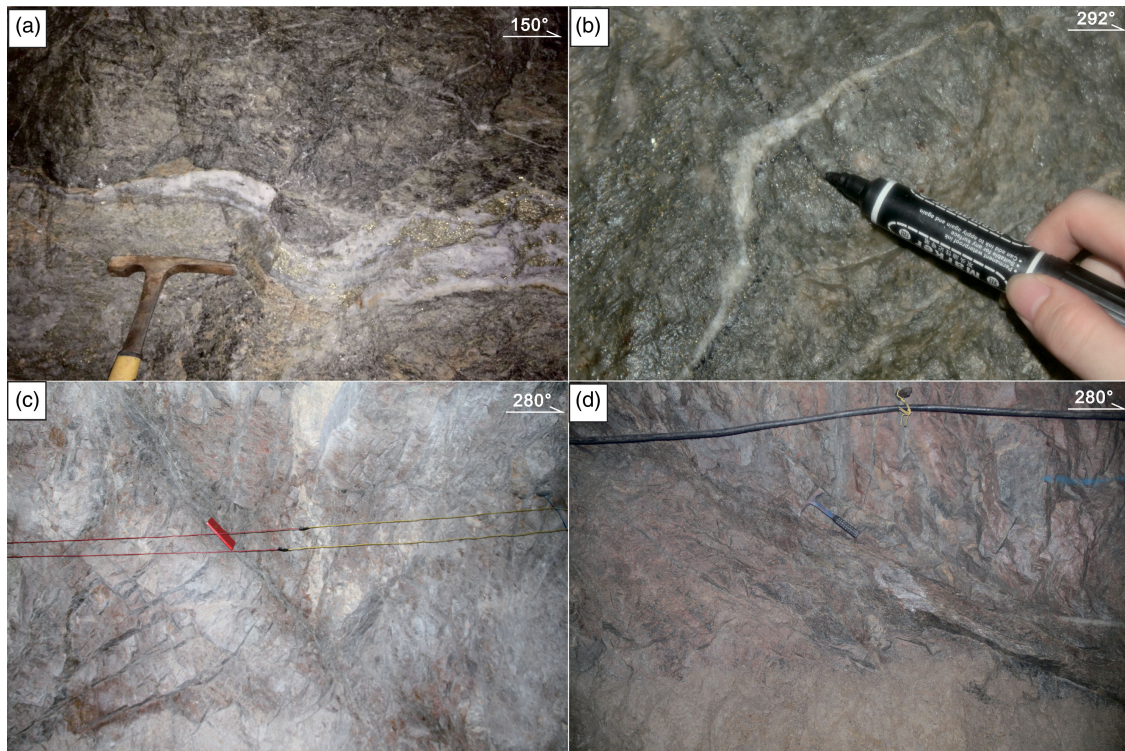


Fig. 6. (Colour online) Field photographs showing the geometry of the quartz veins in the Sizhuang gold deposit. (a) Quartz veins consisting of the curved segments longer than 1 m; (b) quartz veins consisting of curved segments with sharp bends and shorter than 1 m; (c, d) main veins accompanied by offshoots oriented either clockwise or anticlockwise from main veins.

earlier than the quartz veins. Furthermore, some quartz veins with high angles or perpendicular to the dikes occur within the bridge zones formed by the NNE–SSW- ($\sim 0\text{--}042^\circ$) trending dikes (Fig. 3f) but not the dikes trending NNW–SSE ($\sim 310\text{--}355^\circ$) (Fig. 3c, e).

4. Methodology

4.a. Fracture-orientation analysis and stress inversion

The first 3D palaeostress analysis using the dilatant fractures was possible through the technique proposed by Baer *et al.* (1994). This technique extended the two-dimensional (2D) analytical approach of Delaney *et al.* (1986), which was based on the mechanical fundamental that the pre-existing fracture could be opened if P_f exceeds the normal stress (σ_n) acting on its walls (Anderson, 1939). The 3D analytical technique analysed the attitude variations of the dilatant fractures like the dikes and veins by calculating the border of the region of poles to dilatant fractures on a stereographic projection (Baer *et al.* 1994). Later it was improved by the Jolly–Sanderson graphical method (Jolly & Sanderson, 1997). Several recent studies have employed the Jolly–Sanderson method to determine the palaeostress state and the driving fluid pressure (P_f) when dikes or veins formed (Mckeagney *et al.* 2004; Mazzarini & Isola, 2007; Bhatt *et al.* 2019; Goswami *et al.* 2021). For the method, the number density of the poles to the fractures must change abruptly towards the border so that the poles can be readily divided into two domains, one with data points and the other without, on the stereogram (see fig. 3a in Sato *et al.* 2013). The shape and position of the border between the two domains indicate the palaeostress state (Baer *et al.* 1994; Jolly & Sanderson, 1997; Yamaji *et al.* 2010; Sato *et al.* 2013). In many cases, however, the poles show

a nebulous pattern on a stereogram (see fig. 3b in Sato *et al.* 2013), leading to difficulty in identifying the border on the stereogram (Yamaji *et al.* 2010; Sato *et al.* 2013). Solution of the problem has been attempted by numerical modelling methods, including stochastic modelling using the Bingham distribution (Yamaji *et al.* 2010) and the power-law distribution (Sato *et al.* 2013), as well as the non-parametric statistical approach without any stochastic model (Sato *et al.* 2013). However, the above methods are invalid for the fracture orientation data collected from multiple fracturing events (Yamaji & Sato, 2011). For the last case of heterogeneous fracture orientation data, the fuzzy clustering technique, which extended the Bingham stochastic model (Yamaji *et al.* 2010) into a mixed Bingham distribution, was proposed by Yamaji & Sato (2011). This technique has been successfully applied to the Early Miocene dikes in Tsuruga Bay (Sato *et al.* 2013), the Miocene Kuromoritoge dikes in Ishizuchi (Yamaji & Sato 2011), the gold veins in Hishikari Mine, southern Japan (Faye *et al.* 2018), and the quartz veins of Panasqueira Mine (Pascal *et al.* 2022).

4.b. The fuzzy clustering technique

The fuzzy clustering technique of Yamaji & Sato (2011), developed into the Genetic Algorithm included in the software GArCMB proposed by Yamaji (2016), improves on the Jolly–Sanderson graphical method (Jolly & Sanderson, 1997) by enabling 3D palaeostress inversion based on dilatant fractures. The poles to the dilatant fractures formed under a given stress state on a stereographic projection show an orthorhombic distribution, which is either an elliptical cone around σ_3 constrained by angles θ_1 and θ_2 in the case of $P_f < \sigma_2$ (Fig. 8a, d, g), or a girdle normal to

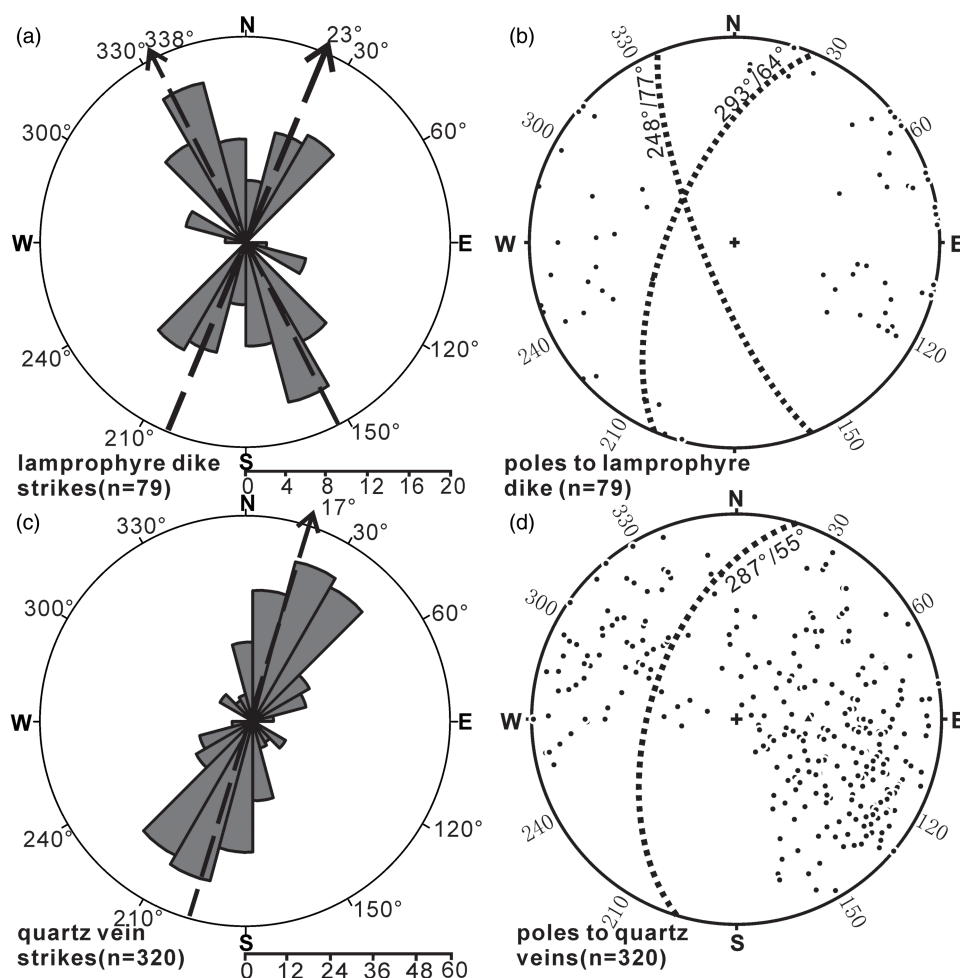


Fig. 7. (a) Rose diagram of 79 dike segments from the Sizhuang gold deposit; dashed lines represent the mean strikes of the two main sets formed by NNW–SSE- and NNE–SSW-trending lamprophyre dikes. (b) lower-hemisphere, equal-area stereogram of poles to 79 dike segments from the Sizhuang gold deposit; dashed great circles represent the mean orientations of dikes trending NNW and NNE. (c) Rose diagram of 320 quartz veins from the Sizhuang gold deposit; the dashed line represents the mean strike of 320 quartz veins. (d) Lower-hemisphere, equal-area stereograms of poles to 320 quartz veins from the Sizhuang gold deposit; dashed great circles represent the mean orientation of 320 quartz veins.

σ_1 constrained by θ_2 and θ_3 when $P_f > \sigma_2$ (Fig. 8b, e, h), except for the double cone constrained by θ_2 with θ_1 and θ_3 being 0° and 90° , respectively, in the special case of $P_f = \sigma_2$ (Fig. 8c, f, i) (Jolly & Sanderson, 1997). Thus, the directions of the principal stress axes σ_1 , σ_2 and σ_3 , the stress ratio $\Phi = (\sigma_2 - \sigma_3)/(\sigma_1 - \sigma_3)$ and the driving pressure ratio $R' = (P_f - \sigma_3)/(\sigma_1 - \sigma_3)$ can be mathematically calculated according to the angles θ_1 and θ_2 , or θ_2 and θ_3 (for details, see Jolly & Sanderson, 1997; Pascal, 2021).

Given the similarity between the distribution of the poles and the dilatant fractures with the same origin and the Bingham distribution (Bingham, 1974), the fuzzy clustering technique employed the Bingham statistics to invert the four parameters of stress tensors and the driving pressure ratio R' based on the orientations of dilatant fractures (Yamaji & Sato, 2011; Pascal *et al.* 2022). The Bingham distribution has three symmetrical axes t_1 , t_2 and t_3 , which represent the minimum, intermediate and maximum concentration axes of the poles on a stereographic projection, respectively, and the pairs of scalars κ_1 and κ_2 ($\kappa_1 \leq \kappa_2 \leq 0$), which refer to the concentration of data points from t_3 to t_1 and from t_3 to t_2 , respectively (see fig. 5.6b in Pascal, 2021). Through the logarithmic likelihood function, the best-fitting Bingham distribution is found; thus, the optimal t_1 , t_2 , t_3 , κ_1 and κ_2 are produced (Yamaji

et al. 2010). Then the three principal stress axes, i.e. $t_1 = \sigma_1$, $t_2 = \sigma_2$ and $t_3 = \sigma_3$, and the stress ratio $\Phi = \kappa_2/\kappa_1$ are directly determined, whereas the driving pressure ratio R' can be determined by the position of the pole of the vein with maximum normal stress imposed on the dilatant fracture in the Mohr space (Pascal, 2021).

In the case of heterogeneous fracture data, the fuzzy clustering technique aims to find a robust mixed Bingham distribution to fit the data by separating the heterogeneous orientation dataset into the optimal number of homogeneous subsets (K^{opt}), using the Bayesian information criterion value (BIC value; Faye *et al.* 2018). The K^{opt} can be obtained by the XY plot on which the abscissa values are K (number of subsets), and the subordinate values are BIC value (see fig. 7a in Faye *et al.* 2018). The BIC values for different possible K (generally $K = 1, 2, 3, 4, 5$) are obtained using GARcmB software (Yamaji, 2016). Based on Yamaji's (2016) principle, at least ten inversion routines for each given K are carried out to ensure the smallest statistical variability. Once the K^{opt} , the K value corresponding to the minimum BIC on the XY plot (see fig. 7a in Faye *et al.* 2018), is defined, the symmetry axes t_1 , t_2 and t_3 , and the concentrations κ_1 and κ_2 of the K^{opt} Bingham components are accurately determined. Thus, the K^{opt} reduced stress tensors are obtained.

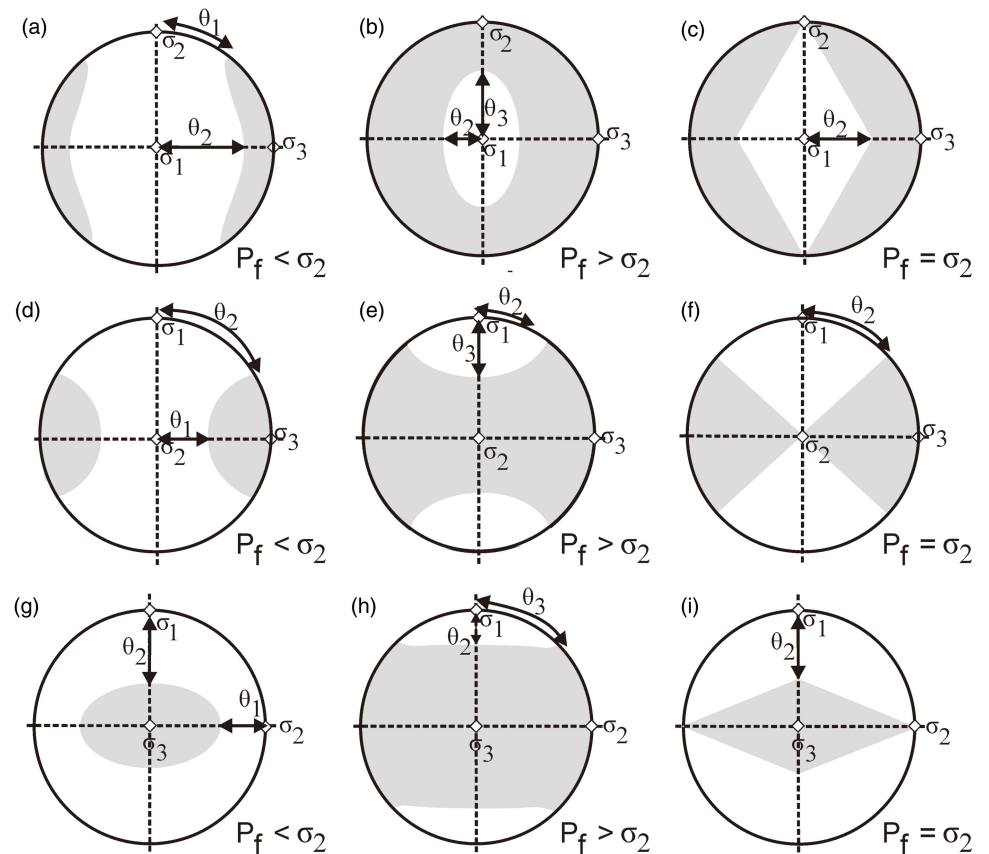


Fig. 8. Equal-area, lower-hemisphere stereogram showing the theoretical distribution of poles to dilatant fractures (grey areas). (a), b, c) for $P_f < \sigma_2$, $P_f > \sigma_2$ and $P_f = \sigma_2$, respectively, for hypothetical cases with vertical σ_1 (modified from Martinez-Poza et al. 2014); (d, e f) for $P_f < \sigma_2$, $P_f > \sigma_2$ and $P_f = \sigma_2$, respectively, for hypothetical cases with vertical σ_2 (method based on Jolly and Sanderson 1997); (g, h, i) for $P_f < \sigma_2$, $P_f > \sigma_2$ and $P_f = \sigma_2$, respectively, for hypothetical cases with vertical σ_3 (method based on Jolly and Sanderson, 1997).

4.c. Phlogopite ^{40}Ar - ^{39}Ar dating

Phlogopite grains of 500–200 μm diameter were separated, applying conventional magnetic and heavy-liquid techniques, from the fresh lamprophyre samples, which were crushed to a grain size of *c.* 30 to 70 mesh, and then were dried in a constant-heat (50 $^{\circ}\text{C}$) oven at Langfang Technology Service Co., Ltd of Geoscience Exploration, Hebei Province, China. Subsequently, they were picked out by hand under a binocular microscope to achieve purity $\geq 99\%$ and then repeatedly washed using deionized water followed by acetone. After the final cleaning with acetone, the phlogopite separations were dried in a thermostat at 50 $^{\circ}\text{C}$. After being weighed, they were loaded into aluminium packets, which were then put into a silicate glass tube (Can UM#84), interleaved with the packets that contained the flux monitor Mount Fish Canyon sanidine with the age of 28.1260 ± 0.0093 Ma (1σ) (Phillips et al. 2017). The canister was then sent to the CLICIT facility of the Oregon State University (USA) TRIGA reactor, to be irradiated for 40 MWhr.

After irradiating them, we removed the mineral separates from their packaging and placed them in a custom-designed copper laser sample tray. ^{40}Ar - ^{39}Ar step-heating analyses were performed on a Thermofisher ARGUSVI multi-collector mass spectrometer according to procedures previously described by Matchan and Phillips (2014). Samples were outgassed using the 6 mm homogenized beam of a Photonmachines Fusions 10.6 CO_2 continuous wave laser operated at low power (1–2 %), and the bulk of atmospheric argon was removed. They were then step-heated over 4–10 % laser power. Blanks were monitored routinely and subtracted from sample measurements.

All the ^{40}Ar - ^{39}Ar isotopic analytical data reported have been corrected for radioactive decay, full-system blanks, nucleogenic interferences, mass discrimination and atmospheric contamination. Throughout the calculations, the total decay constant for ^{40}K of $5.543 \times 10^{-10} \text{a}^{-1}$ (Steiger & Jager, 1977) is applied, and the values for the Ca and K correction factors are $(2.6580 \pm 0.0024) \times 10^{-4}$ for $(^{36}\text{Ar}/^{37}\text{Ar})_{\text{Ca}}$ and $(6.716 \pm 0.018) \times 10^{-4}$ for $(^{39}\text{Ar}/^{37}\text{Ar})_{\text{Ca}}$, and $(3.17 \pm 0.25) \times 10^{-4}$ for $(^{40}\text{Ar}/^{39}\text{Ar})_{\text{K}}$ and $(1.2819 \pm 0.0002) \times 10^{-2}$ for $(^{38}\text{Ar}/^{39}\text{Ar})_{\text{K}}$, respectively. The irradiation factor for the phlogopite aliquot was $J = 0.00911937 \pm 0.00000192$, obtained according to the age of 28.1260 ± 0.0093 Ma (1σ) for FC sanidine (Phillips et al. 2017). For the isochron interpretation and discrimination calculation, the value of 298.56 ± 0.31 for the present-day atmospheric argon (Lee et al. 2006) was employed. All errors are reported as 1σ .

5. Palaeostress analysis and age of the lamprophyre dikes and quartz veins

5.a. The stresses for lamprophyre dikes

The poles to the lamprophyre dikes, as projected in a contoured stereogram (1 % contour per 1 % area) (Fig. 9a), show an overall clustered distribution with two distinct maximum concentration orientations. These concentrations correspond to two sets of symmetry axes (Fig. 9a) that imply the existence of two main sets for the lamprophyre dikes in the Sizhuang gold deposit, i.e. those trending NNW–SSE and NNE–SSW. We applied the fuzzy clustering technique not only for $K = 2$, i.e. two clusters, but for testing

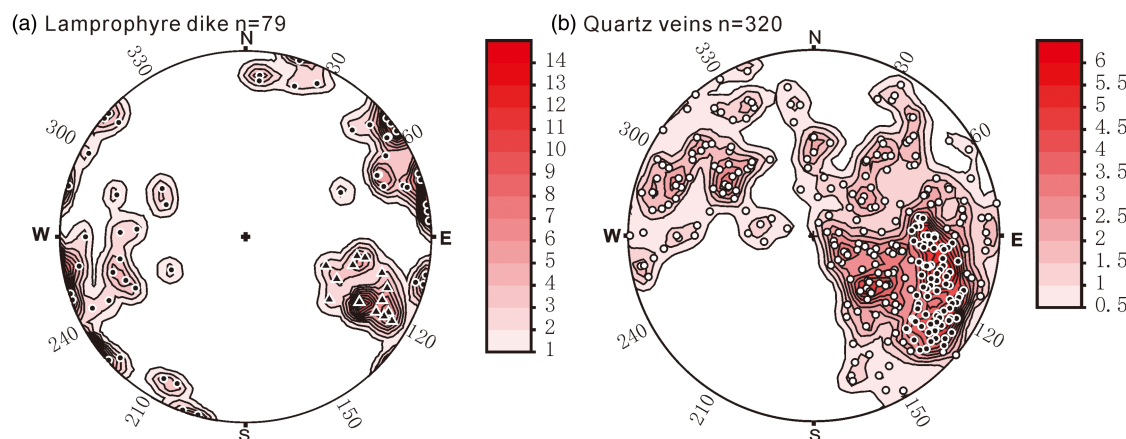


Fig. 9. (Colour online) (a) Contoured lower-hemisphere equal-area projection of poles to 79 dike segments from the Sizhuang gold deposit, showing two distinct clusters indicated by the solid black circles and the solid black triangles, respectively. (b) Contoured lower-hemisphere equal-area projection of poles to 320 quartz veins from the Sizhuang gold deposit, showing the overall distribution of a girdle type except that there is a significant cluster of poles indicated by the solid black circles in the northeast.

K values from 1 to 5 with the aid of software GArCmB (Yamaji, 2016). As a result, we can test which K value provides the minimum BIC value, i.e. the optimum value. Among the obtained BIC values in the XY plot, the minimum value is when $K = 2$ (Fig. 10a), thus indicating that two homogeneous clusters, A and B, better describe the recorded data. Accordingly, these clusters define two stress states, LDA and LDB, with the ω values equal to 0.76 and 0.24, respectively, explaining the emplacement of 76 % and 24 % of the lamprophyre dikes under stresses LDA and LDB, respectively.

However, whether a dike was deposited under stress LDA or LDB depends on its memberships, which are denoted by the probability of belonging to clusters A and B. The memberships are indicated by gradation between black and white circles on the equal-area projection (Fig. 10b), each of which has a value between 0 and 1. Dikes deposited under stress LDA are shown with solid black circles in Figure 10b, the membership of which to cluster A is 1; whereas the dikes formed under stress LDB are shown with solid coloured to open white circles in Fig. 10b, the membership of which to cluster A is <1 . Stress LDA was an extensional stress regime with the attitudes of σ_1 , σ_2 and σ_3 axes at 151–168°, 338–322° and 247–203°, respectively, and $\Phi = 0.50$ (Fig. 10b). Stress LDB was a strike-slip regime with the attitudes of σ_1 , σ_2 and σ_3 axes at 215–217°, 334–359° and 117–126°, respectively, and $\Phi = 0.16$ (Fig. 10b). The two groups showed the driving pressure R' values at 0.47 and 0.06, respectively (Fig. 10c, d).

5.b. The stresses for quartz veins

For the 320 quartz vein orientation data, the BIC is minimum at $K = 1$ (Fig. 11a). Therefore, a single stress regime, called QVA (Fig. 11b), can explain all the orientations. QVA defines an inclined stress state with the attitudes of σ_1 , σ_2 and σ_3 axes at 212–21°, 326–47° and 106–36°, respectively, and $\Phi = 0.40$ (Fig. 11b, c). The driving pressure R' value is high at 0.75. The stress QVA is consistent with the fact that the poles to the quartz veins, lying inside the 0.5 % contour per 1 % area in the contoured diagram, show the overall distribution of a girdle type with $P_f > \sigma_2$ (Fig. 9b).

However, it should be noted that there is a significant cluster of poles in the northeast (Fig. 9b), suggesting that a great number of quartz veins strike NNE–SSW with dips towards NW (mean orientation of 287–55°; Fig. 7d). These veins are the largest, with no slickenlines, forming bands (Fig. 5d–f) (sub)parallel to the

NNE–SSW lamprophyre dikes, indicating that the dilation of NNE–SSW fractures was not only at high P_f but also at low P_f . More interestingly, the distribution of the poles lying within the 3 % contour includes 81 orientation data (solid black circles), accounting for 25 % of the quartz veins, and has different symmetry axes from those of the overall girdle-type distribution (Fig. 9b), indicating changes in the state of stress during the vein emplacement (Tran & Ravooof, 2007; Mondal & Mamtani, 2013). The clustered distribution indicates low P_f ($P_f < \sigma_2$).

For the clustered distribution, the BIC is minimum at $K = 1$ (Fig. 11d). The obtained stress regime, called QVB (Fig. 11e), has the attitudes of σ_1 , σ_2 and σ_3 axes at 238–46°, 004–29°, and 112–29°, respectively, and $\Phi = 0.16$ (Fig. 11e, f). The driving pressure R' value is low at 0.09, suggesting that whenever P_f is of magnitude almost equal to σ_3 stress, the formed veins are perpendicular to the σ_3 axis, which is consistent with the fact that only a very limited number of vein poles lie to the left of the P_f line (Fig. 11f).

5.c. Comparison of stresses (for lamprophyre dikes and quartz veins)

Two stress states have been defined by the lamprophyre dikes, and two stress states by the quartz veins, using the fuzzy clustering technique of Yamaji & Sato (2011). These four stress states indicate similarities and differences, and because of this, herein, we attempt to clarify better and unify these results. In total, three different stress regimes are defined (Table 1):

- (1) Stress regime A (i.e. LDA). Only the lamprophyre dikes define it. It has a sub-vertical σ_1 axis, and sub-horizontal ENE–WSW-trending σ_3 axis (Fig. 10b, c), indicating an extensional stress regime with obtained stress ratio values defining Radial–Pure extension to Pure Extension stress regimes (stress types based on Tranos *et al.* 2008), under which P_f was lower unless almost equal to σ_2 .
- (2) Stress regime B (i.e. LDB and QVB). This is the main stress state defined by the clustered distribution of the lamprophyre dikes and quartz veins (Figs 10b, d, 11e, f). This stress regime is characterized by the more stable position of the σ_3 axis, which plunges towards the ESE at low angles, i.e. between the trends of the least principal stress axes of the ST1 and ST2 stress regimes (see Section 5.d for details). Although σ_1 and σ_2 axes

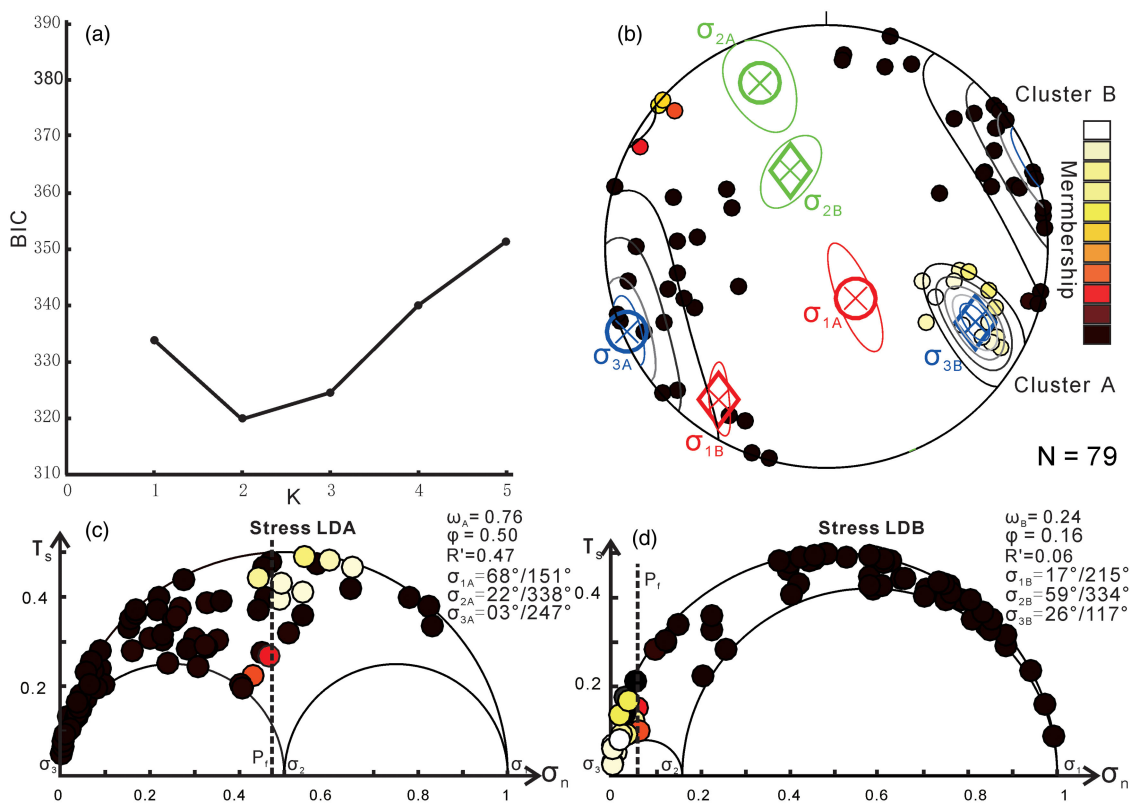


Fig. 10. (Colour online) Palaeostress analysis based on the lamprophyre dike orientation data with the fuzzy clustering technique. (a) The lamprophyre dike orientation data show the minimum BIC at $K = 2$, meaning that the dike orientations should be partitioned into two clusters. The stresses corresponding to the clusters are called stresses LDA and LDB. (b) Equal-area projection of the poles to the lamprophyre dikes. The colour of a datum point indicates the membership of the orientation. The stress axes are indicated by the circles with crosses for stress LDA and the diamonds with crosses for stress LDB, which centre their 95% error ellipses. The optimal stresses have a stress ratio of 0.50 for stress LDA and 0.16 for stress LDB. (c, d) Mohr circles of the stresses and the normalized normal and shear stresses on the vein walls exerted by the stresses. The colour of each datum point indicates the membership of the datum. The dark line defines P_f .

vary in position along the principal stress σ_1 – σ_2 plane (see LDB in Fig. 10b and QVB in Fig. 11e), the defined stress ratio Φ and driving pressure R' are similar. Because of this, it is better described as an inclined (or oblique) strike-slip stress regime fitting with a transtension stress regime, under which, P_f magnitude was very low, much smaller in magnitude than σ_2 .

- (3) Stress regime C (i.e. QVA). Only the quartz veins define it. Although the calculated σ_3 axis, plunging towards the ESE at low angles, is the same as that in stress regime B, stress regime C has higher Φ and R' , and P_f was also high, i.e. higher than σ_2 . Furthermore, the σ_1 and σ_2 axes are both inclined, defining an inclined (or oblique) stress regime fitting with a transtension stress regime.

5.d. Fault-slip data inversion and stress inversion

In order to accomplish a complete analysis concerning the palaeostresses in the Sizhuang gold deposit, we tried to define them from the fault-slip data in addition to using the dikes and veins. For this purpose, we applied a stress inversion to the available fault-slip data from stations in Jiaolai Basin located closest to the mine area (Fig. 1b), as these fault-slip data have recently been published by B Zhang *et al.* (2020). Those authors, based on their palaeostress analysis and reconstruction, conclude that the Jiaolai Basin has been subjected to six stress regimes since the Cretaceous.

Among them, four extensional regimes are defined: (a) an E–W extension during 135–121 Ma, controlling the formation of the Laiyang Group, (b) a NW–SE extension between 120 and 93 Ma, controlling the formation of the Qiangshan Group, (c) a N–S extension from 85 to 60 Ma, controlling the formation of the Wangshi Group, and (d) a NE–SW extension later than 55 Ma. In the catalogue of B Zhang *et al.* (2020), the fault-slip data stations located closest to the Sizhuang gold deposit are K1Ly-05, K1Ly-06, K1Ly-07, K1Ly-10, K1Ly-25 and K1Ly-27 within the Laiyang Group (Fig. 1b). They include 97 fault-slip data, which are heterogeneous since the area experienced multiple deformation events (B Zhang *et al.* 2020). Because the fault-slip data are heterogeneous, we applied the TR method (TRM) (Tranos, 2015), which was deployed to separate heterogeneous fault slip data into homogeneous groups and define either *in situ* or bulk Andersonian stress tensors for each of these groups.

The TRM is a simple graphical and semi-automatic method plotting the heterogeneous fault-slip data on TR diagrams and defining the slips on the faults, which are simultaneously compatible with a specific orientation of the Andersonian stress axes and a specific stress ratio R ($R = (\sigma_2 - \sigma_3)/(\sigma_1 - \sigma_3)$ with $0 \leq R \leq 1$) (for details, see Tranos, 2015). Stress ratio (R) equals Φ . These faults are called Tensor Ratio Compatible Faults (TRCF), and the optimal TRM stress tensor is the one that explains the largest number of the TRCF with $MA \leq 20^\circ$ and secondly provides the smallest Mean Misfit Angle (MMA).

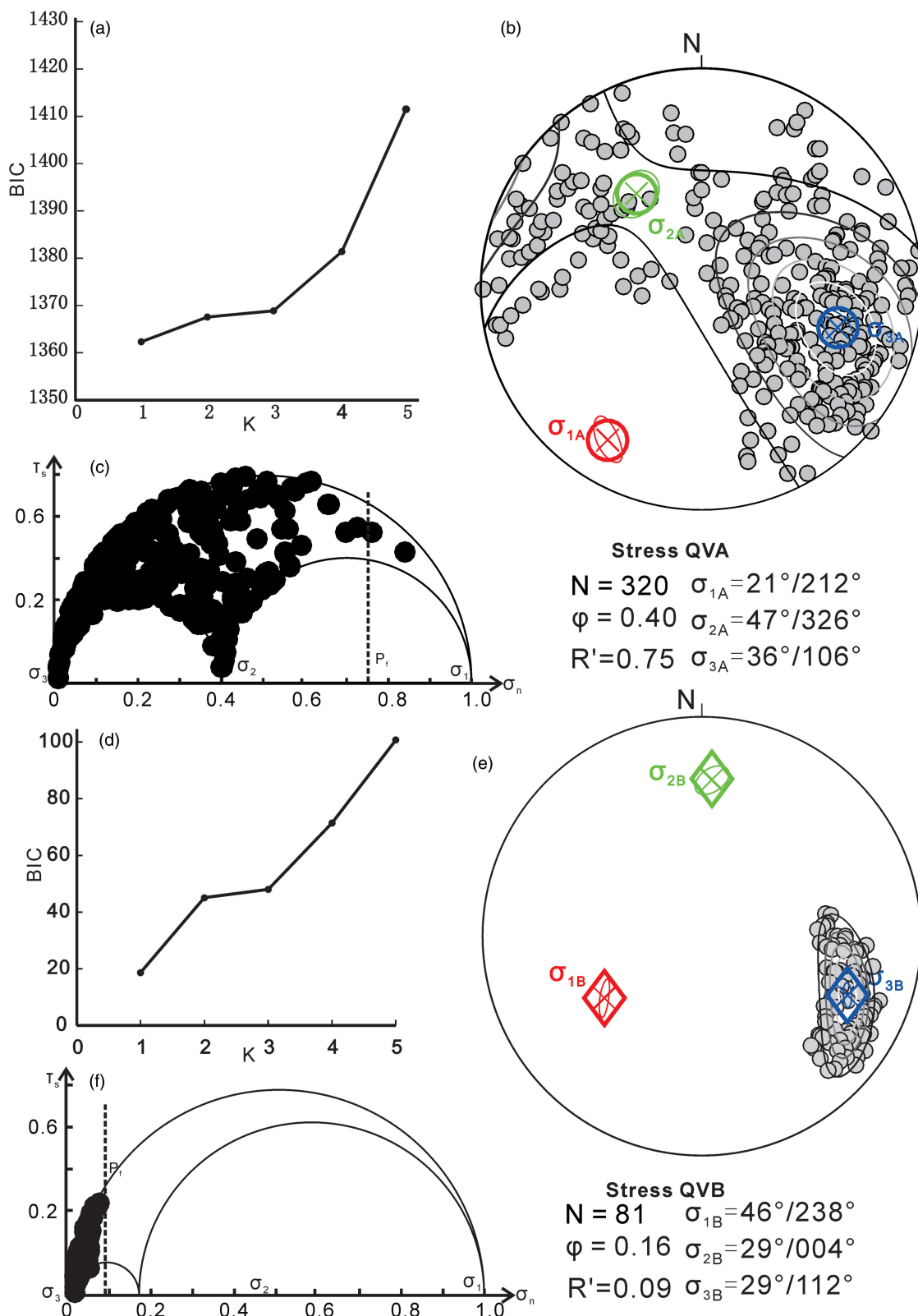


Fig. 11. (Colour online) Palaeostress analysis based on the quartz vein orientation data with the fuzzy clustering technique. (a) The quartz vein orientation data show the minimum BIC at $K = 1$, meaning that a single stress state QVA-FC explains all the vein orientations. (b) Equal-area projection of the poles to the quartz veins. The stress axes are indicated by the circles with crosses, which centre their 95% error ellipses. The optimal stress has a stress ratio of 0.40. (c) Mohr circles of the stress and non-dimensional normal and shear stresses on the vein walls. The dark line defines P_f . (d) For the clustered distribution in Figure 9b, the BIC is minimum at $K = 1$. (e) Equal-area projection of the poles to the quartz veins belonging to the clustered distribution. The stress axes are indicated by the diamonds with crosses, which centre their 95% error ellipses. The optimal stress has a stress ratio of 0.20. (f) Mohr circles of the stress and non-dimensional normal and shear stresses on the vein walls. The dark line defines P_f .

Table 1. Palaeostress analysis results from the lamprophyre dike and quartz vein orientation data in the Sizhuang gold deposit, Jiaodong Peninsula

Stress regime	Stress state	Type of dilatant fracture	σ_1	σ_2	σ_3	ϕ	R'
A	LDA	Lamprophyre dike	151–68°	338–22°	247–03°	0.5	0.47
B	LDB	Lamprophyre dike	215–17°	334–59°	117–26°	0.16	0.06
	QVB	Quartz vein	238–46°	004–29°	112–29°	0.16	0.09
C	QVA	Quartz vein	212–21°	326–47°	106–36°	0.4	0.75

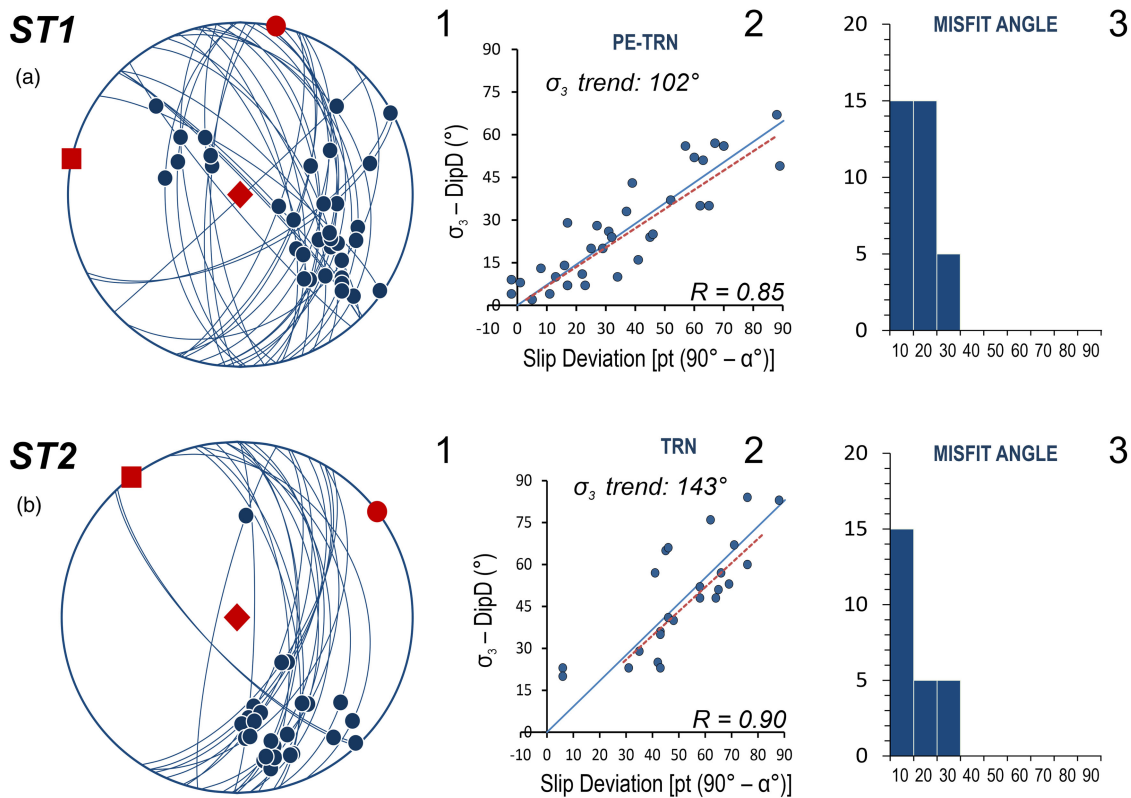


Fig. 12. (Colour online) Results of the TRM application (Tranos, 2015) on the recently published fault-slip data by B Zhang *et al.* (2020). The optimal resolved stress tensors (a) ST1 and (b) ST2. Explanation: 1. Equal-area, lower-hemisphere projection of the TR-compatible fault slip data. σ_1 , σ_2 and σ_3 axes are shown with solid red rhomb, circle and square, respectively; 2. TR diagram showing the TR-compatible faults (blue balls), the 'real' (blue line) and 'theoretical' (red dashed line) Final Tensor Ratio Lines (for details, see Tranos, 2015); R is the stress ratio; 3. Misfit angle distribution of the TR-compatible faults.

Applying the TRM on the 97 fault-slip data, two extensional bulk stress tensors, ST1 (Fig. 12a) and ST2 (Fig. 12b), are defined. The former has attitudes for σ_1 : 102–90°, σ_2 : 012–00°, σ_3 : 102–00° and $R = 0.85$ from 35 TRCF with $\leq 30^\circ$, 30 with $MA \leq 20^\circ$ and $MMA = 12.9^\circ$; and the second has attitudes for σ_1 : 143–90°, σ_2 : 053–00°, σ_3 : 143–00° and $R = 0.9$ from 25 TRCF with $\leq 30^\circ$, 20 with $MA \leq 20^\circ$ and $MMA = 11.8^\circ$. Although their stress ratios are very similar, based on the percentages of the Stress Tensor Discriminator Faults (STDF), i.e. the faults activated by either A or B stress tensor, but not from both (Tranos, 2015, 2017), they are different stress tensors since these percentages are more than 70 % (Tranos, 2015, 2017). In particular, three STDF percentages were calculated: 92.9 % for the unified ST1 and ST2, 88.6 % for the ST1, and 84.0 % for the ST2 fault-slip datasets, respectively.

ST1 and ST2 stress tensors define an ~E–W pure extension – transension (PE-TRN) and a NW–SE transension (TRN) stress regime, respectively (stress type classification according to Tranos *et al.* 2008).

5.e. Phlogopite ^{40}Ar – ^{39}Ar ages

Two phlogopite aliquots from each sample of the lamprophyre dikes were carried out to examine the reproducibility of the ^{40}Ar – ^{39}Ar ages. Table 2 shows all the isotopic analytical data for each increment. All samples' apparent age spectra and ages, including the plateau ages, total fusion ages and isochron ages, are presented in Figure 13a, b, c, d, f, g, h. If no plateau ages are defined, pseudo-plateau ages are shown (Fig. 13e). All the age errors, derived from the uncertainties in the J value and the irradiation correction factor without including the potassium decay constant, are given with a 95 % confidence level (2σ). Plateau ages are the weighted mean of a sequence of consecutive, concordant step ages, indistinguishable at the 95 % confidence level and encompassing over 50 % of the total ^{39}Ar gas released (Dallmeyer & Lecorche, 1990).

In contrast, pseudo-plateau ages are the weighted mean of contiguous step ages consistent within 2σ , which account for at least 30 % of the total ^{39}Ar gas released (Bi & Zhao, 2017). Total

Table 2. Phlogopite ⁴⁰Ar–³⁹Ar step-heating isotopic analytical results for the lamprophyre dike from the Sizhuang gold deposit, Jiaodong Peninsula

Step No.	Laser (Watt)	⁴⁰ Ar/ ³⁹ Ar	³⁸ Ar/ ³⁹ Ar	³⁷ Ar/ ³⁹ Ar	³⁶ Ar/ ³⁹ Ar	⁴⁰ *Ar/ ³⁹ Ar	% ⁴⁰ Ar*	Age (Ma)	±2σ(Ma)	⁴⁰ Ar Moles	³⁹ Ar Moles	³⁸ Ar Moles	³⁷ Ar Moles	³⁶ Ar Moles
Sample number: SZ16D004B1; Aliquot: WZL1-1; Mineral: Phlogopite 5 grains; J-value = 0.00911937 ± 0.00000192 (0.021%; 1σ)														
1	1.0%	10.9434	0.00292	1.67217	0.01549	6.3186	57.737	101.07	1.3	51.175	4.67634	0.01365	7.81964	0.07244
2	1.5%	8.9488	0.00083	0.13502	0.00441	7.6310	85.270	121.37	0.5	112.570	12.57927	0.01047	1.69851	0.05553
3	2.0%	8.5181	0.00063	0.00449	0.00332	7.5262	88.353	119.76	0.3	177.264	20.81029	0.01303	0.09345	0.06913
4	2.5%	8.2019	0.00044	0.00284	0.00233	7.5062	91.515	119.45	0.2	270.296	32.95530	0.01447	0.09347	0.07679
5	3.0%	7.9777	0.00030	0.00296	0.00159	7.5045	94.064	119.42	0.2	252.232	31.61704	0.00945	0.09350	0.05011
6	4.0%	7.9565	0.00028	0.00151	0.00149	7.5104	94.389	119.51	0.1	493.395	62.01151	0.01747	0.09352	0.09266
7	4.5%	7.8121	0.00020	0.00253	0.00105	7.4985	95.982	119.33	0.2	289.218	37.02197	0.00733	0.09354	0.03888
8	5.5%	7.7827	0.00018	0.00143	0.00098	7.4903	96.238	119.20	0.2	508.199	65.29849	0.01206	0.09357	0.06396
9	7.0%	7.6810	0.00013	0.00187	0.00068	7.4787	97.362	119.03	0.1	384.090	50.00501	0.00639	0.09359	0.03389
10	10.0%	7.6589	0.00011	0.00138	0.00056	7.4921	97.819	119.23	0.1	521.051	68.03241	0.00716	0.09361	0.03799
11	13.0%	7.5878	0.00007	0.00377	0.00037	7.4781	98.551	119.02	0.3	188.430	24.83334	0.00172	0.09365	0.00912
12	15.0%	7.6043	0.00008	0.01228	0.00045	7.4703	98.234	118.90	0.6	58.009	7.62850	0.00065	0.09367	0.00342
Sample number: SZ16D004B1; Aliquot: WZL1-2; Mineral: Phlogopite 5 grains; J-value = 0.00911937 ± 0.00000192 (0.021%; 1σ)														
1	2.0%	9.1333	0.00106	0.07309	0.00564	7.4505	81.572	118.59	0.3	290.140	31.76715	0.03375	2.32191	0.17905
2	3.0%	7.8249	0.00019	0.02062	0.00103	7.5185	96.080	119.64	0.1	462.433	59.09725	0.01143	1.21854	0.06066
3	4.0%	7.7642	0.00017	0.01533	0.00091	7.4931	96.504	119.25	0.1	802.359	103.34021	0.01769	1.58374	0.09385
4	5.0%	7.7098	0.00014	0.00103	0.00077	7.4805	97.022	119.05	0.1	700.330	90.83682	0.01315	0.09379	0.06976
5	6.0%	7.6712	0.00012	0.00124	0.00061	7.4888	97.619	119.18	0.1	582.669	75.95555	0.00875	0.09381	0.04640
6	8.0%	7.6514	0.00010	0.00119	0.00055	7.4875	97.854	119.16	0.1	601.114	78.56288	0.00813	0.09382	0.04312
7	10.0%	7.6971	0.00012	0.01142	0.00064	7.5066	97.520	119.45	0.3	116.051	15.07709	0.00181	0.17221	0.00962
8	15.0%	7.6259	0.00006	0.30612	0.00032	7.5293	98.728	119.80	1.4	31.104	4.07870	0.00025	1.24857	0.00132
Sample number: SZ16D002B2; Aliquot: WZL2-1; Mineral: Phlogopite 20 grains; J-value = 0.00911937 ± 0.00000192 (0.021%; 1σ)														
1	1.0%	9.9981	0.00244	0.01241	0.01292	6.1394	61.403	98.28	2.5	19.624	1.96278	0.00478	0.02437	0.02537
2	1.5%	8.7097	0.00075	0.01957	0.00401	7.5139	86.268	119.57	0.9	42.401	4.86829	0.00368	0.09527	0.01950
3	2.0%	8.1554	0.00039	0.01163	0.00207	7.5387	92.435	119.95	0.6	66.825	8.19391	0.00319	0.09528	0.01692
4	2.5%	7.8716	0.00022	0.05900	0.00118	7.5204	95.534	119.67	0.7	46.101	5.85661	0.00130	0.34554	0.00689
5	3.0%	7.9372	0.00027	0.03250	0.00141	7.5153	94.681	119.59	0.5	83.397	10.50713	0.00280	0.34146	0.01485
6	3.5%	7.8066	0.00019	0.05400	0.00102	7.5011	96.082	119.37	0.6	72.542	9.29242	0.00179	0.50176	0.00951

(Continued)

Table 2. (Continued)

Step No.	Laser (Watt)	⁴⁰ Ar/ ³⁹ Ar	³⁸ Ar/ ³⁹ Ar	³⁷ Ar/ ³⁹ Ar	³⁶ Ar/ ³⁹ Ar	⁴⁰ *Ar/ ³⁹ Ar	% ⁴⁰ Ar*	Age (Ma)	±2σ(Ma)	⁴⁰ Ar Moles	³⁹ Ar Moles	³⁸ Ar Moles	³⁷ Ar Moles	³⁶ Ar Moles
7	4.0%	7.6986	0.00012	0.02506	0.00063	7.5113	97.563	119.53	1.0	29.298	3.80565	0.00045	0.09537	0.00239
8	5.0%	7.7134	0.00015	0.27109	0.00080	7.4742	96.895	118.96	1.0	42.134	5.46248	0.00082	1.48081	0.00438
9	6.0%	7.6387	0.00012	0.19501	0.00065	7.4445	97.453	118.50	0.8	55.070	7.20929	0.00088	1.40590	0.00469
10	8.0%	7.6916	0.00014	0.08430	0.00072	7.4778	97.216	119.01	0.5	78.666	10.22752	0.00138	0.86214	0.00732
11	15.0%	7.7463	0.00017	0.06300	0.00093	7.4695	96.423	118.88	0.5	79.149	10.21767	0.00179	0.64369	0.00947
Sample number: SZ16D002B2; Aliquot: WZL2-2; Mineral: Phlogopite 20 grains; J-value = 0.00911937 ± 0.00000192 (0.021%; 1σ)														
1	1.5%	9.1792	0.00125	0.17000	0.00662	7.2013	78.450	114.75	0.9	60.673	6.60981	0.00825	1.12369	0.04379
2	2.0%	8.0273	0.00028	0.08718	0.00151	7.5778	94.397	120.55	0.6	71.384	8.89265	0.00252	0.77527	0.01339
3	2.5%	7.8582	0.00020	0.06669	0.00105	7.5459	96.022	120.06	0.6	69.581	8.85452	0.00175	0.59052	0.00926
4	3.0%	7.7949	0.00017	0.00798	0.00088	7.5335	96.643	119.87	0.4	93.324	11.97253	0.00198	0.09559	0.01048
5	3.5%	7.7344	0.00014	0.10927	0.00073	7.5175	97.192	119.62	0.7	54.791	7.08409	0.00097	0.77410	0.00515
6	4.5%	7.7039	0.00013	0.07788	0.00069	7.4987	97.333	119.33	0.4	92.528	12.01061	0.00156	0.93542	0.00825
7	5.5%	7.5972	0.00008	0.29876	0.00042	7.4714	98.340	118.91	0.8	45.912	6.04331	0.00048	1.80550	0.00255
8	6.5%	7.5836	0.00008	0.25734	0.00042	7.4582	98.342	118.71	0.6	54.640	7.20496	0.00057	1.85414	0.00303
9	8.0%	7.5602	0.00006	0.22856	0.00030	7.4696	98.798	118.89	0.5	72.653	9.60993	0.00055	2.19647	0.00292
10	10.0%	7.5580	0.00005	0.24240	0.00026	7.4808	98.974	119.06	0.6	54.972	7.27332	0.00035	1.76305	0.00188
11	15.0%	7.6057	0.00006	0.05080	0.00031	7.5128	98.774	119.55	0.8	49.851	6.55438	0.00038	0.33294	0.00204
12	20.0%	7.6686	0.00013	0.72004	0.00070	7.4597	97.272	118.73	2.5	13.190	1.71996	0.00023	1.23845	0.00120

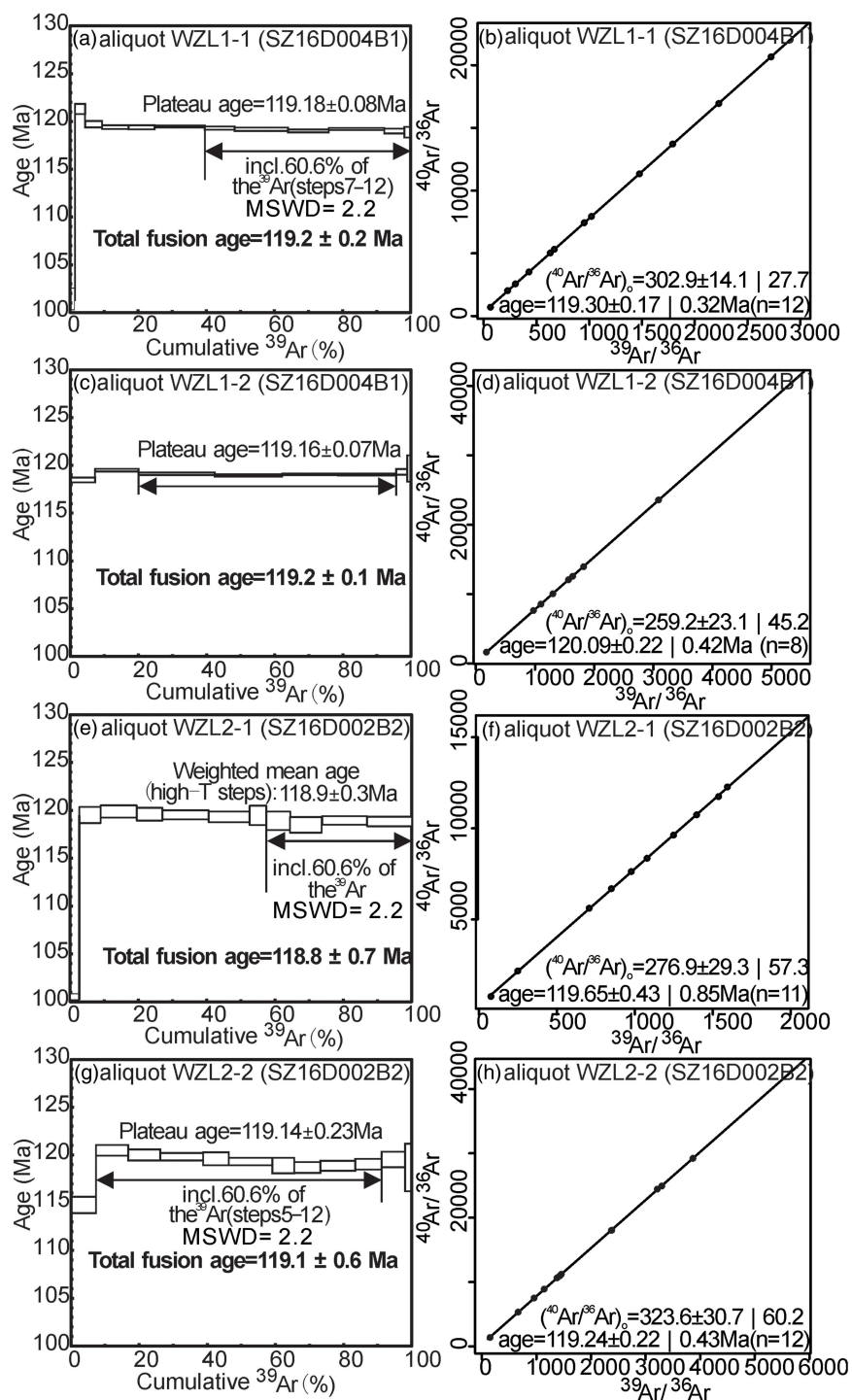


Fig. 13. Phlogopite ^{40}Ar - ^{39}Ar plateau (a, c, e, g) and isochron ages (b, d, f, h) for the lamprophyre dike from the Sizhuang gold deposit. (a, b) Aliquot WZL1-1 from sample SZ16D004B1; (c, d) aliquot WZL1-2 from sample SZ16D004B1; (e, f) Aliquot WZL2-1 from sample SZ16D002B2; (g, h) aliquot WZL2-2 from the sample.

fusion ages and isochron ages are obtained by adding all step ages to derive a single total gas age and from the slope of the line best fitted to plateau-forming step compositions using a least-squares regression (York, 1969), respectively. All the isochron plots (Fig. 13b, d, f, h) commonly show the initial $^{40}\text{Ar}/^{36}\text{Ar}$ ratios identical or close within error to the value of 298.56 ± 0.31 for the present-day atmospheric argon (Lee *et al.* 2006), meaning that the non-atmospheric initial argon (excess argon) has no significant effect on our samples.

Three of four phlogopite aliquots, comprising WZL1-1 and WZL1-2 from sample SZ16D004B1, and WZL2-2 from sample SZ16D002B2, show the ideal flat spectra encompassing 60.6%, 76%, and 61.3% of the released total ^{39}Ar , yielding the well-defined high precision plateau ages of 119.18 ± 0.08 Ma, 119.16 ± 0.07 Ma, and 119.14 ± 0.23 Ma, respectively (Fig. 13a, c, e). These well-defined plateau ages of individual phlogopite aliquots are reproducible with respective total fusion ages (Fig. 13a, c, e). In addition, the three phlogopite aliquots produce the isochron ages consistent

with their respective plateau ages (Fig. 13b, d, h). Therefore, the well-defined high-precision plateau ages, as well as the reproducibility of the plateau, total fusion and isochron ages, imply that the effect of minor argon loss, indicated by the relatively younger ages in the initial steps (Fig. 13a, c, e), is not significant.

The other phlogopite aliquot, WZL2-1 from sample SZ16D002B2, has somewhat perturbed age spectra (Fig. 13e). However, a pseudo-plateau age of 118.9 ± 0.3 Ma is given by 8 to 11 steps with *c.* 42.7 % of the released total ^{39}Ar . It is also reproducible with both the total fusion age at 118.8 ± 0.7 Ma (Fig. 13e) and the isochron age of 119.65 ± 0.43 Ma (Fig. 13f). Furthermore, the pseudo-plateau age is indistinguishable from the plateau age of aliquot WZL2-2 from the same sample SZ16D002B2 (Fig. 13e, g) and thus is considered to be geologically meaningful.

Different samples collected from the fresh and non-deformed NNE–SSW-trending lamprophyre dikes, which are moderately and steeply dipping, respectively, have plateau ages that are reproducible within uncertainties, meaning that these lamprophyre dikes formed in a single, short-lived magmatic event.

6. Discussion

The lamprophyre dikes and quartz veins in the Sizhuang gold deposit have various geometric properties regarding their orientations and sizes, revealing a complex deformational history. The lamprophyre dikes and quartz veins are dilational with mineral crystals normal to their generally rough wall surfaces in their majority. As we already mentioned, dikes are strongly affected by the mechanical properties of their host rocks and, more precisely, the host-rock lithology, stress field and pre-existing fractures (Pollard *et al.* 1975; Baer, 1991). Previous studies have revealed that *c.* 90 % of the lamprophyre dikes trend from azimuths 0° to 040° (Li *et al.* 2016), i.e. parallel to the Jiaojia Fault and the dominant Mesozoic tectonic fabric in the Jiaodong Peninsula, and only a small proportion of them trend NNW–SSE (Li *et al.* 2016).

In contrast, the lamprophyre dikes in the Sizhuang gold mine are grouped into two major sets and a subsidiary one. The two main sets trend NNW–SSE and NNE–SSW, respectively, whereas a subsidiary set trends WNW–ESE. Although with various dips, the quartz veins mainly trend similarly to the NNE–SSW-trending lamprophyre dikes, suggesting their formations were penecontemporaneous. However, the quartz veins cut across the NNW–SSE-trending lamprophyre dikes sharply, indicating that the latter were formed relatively earlier than the quartz veins and the NNE–SSW-trending lamprophyre dikes. Therefore, the well-defined and high-precision plateau ages of 119.18 ± 0.08 Ma, 119.16 ± 0.07 Ma and 119.14 ± 0.23 Ma, obtained herein by the phlogopite ^{40}Ar – ^{39}Ar dating on the NNE–SSW-trending lamprophyre dikes, indicate that the quartz veins and the NNE–SSW-trending lamprophyre dikes were formed at *c.* 119 Ma.

Furthermore, L Zhang *et al.* (2020) performed the ^{40}Ar – ^{39}Ar dating of muscovite from the quartz–sericite–pyrite altered granite in the Sizhuang deposit, which was cut by the lamprophyre dikes and the quartz veins. It has been well accepted that sericite and muscovite are both susceptible to isotopic resetting during thermal events and deformation (Chesley *et al.* 1999), as was verified by the widely divergent isotopic ages between 133 and 108 Ma by the ^{40}Ar – ^{39}Ar dating of the sericite or muscovite in the gold deposits in the Jiaodong Peninsula (Li *et al.* 2006; Zhang *et al.* 2003; LQ Yang *et al.* 2014; L Zhang *et al.* 2020). Therefore, it is unclear if the sericite or muscovite may have suffered later modifications. Accordingly, given the cutting relations between the lamprophyre

dikes and quartz–sericite–pyrite altered granite in the Sizhuang deposit, the age of 120.5 ± 0.9 Ma by the ^{40}Ar – ^{39}Ar dating of muscovite from the quartz–sericite–pyrite altered granite (L Zhang *et al.* 2020) probably reflects the emplacement age of the NNW–SSE-trending lamprophyre dikes; whereas the 120.1 ± 0.9 Ma (L Zhang *et al.* 2020) overlaps with, within analytical uncertainties ($\pm 2\sigma$), the emplacement age of the NNE–SSW-trending lamprophyre dikes in the Sizhuang deposit.

The analysis and stress inversion of the available fault-slip data recorded close to the area of the Sizhuang gold deposit with the TRM defines two stress regimes, ST1 and ST2, which fit, respectively, in orientation with stress A (E–W extension during 135–121 Ma) and stress B (NW–SE extension between 120 and 93 Ma), as the latter were defined by B Zhang *et al.* (2020). Based on the dating provided by those authors, ST1 is relatively older than ST2, indicating that the least principal stress axis rotated from E–W to NW–SE and the PE–TRN changed progressively to the TRN, under which the strike-slip tectonics is more prevalent. In addition, under the ST1, the trend of the activated fault is NNW–SSE, whereas under the ST2 the activated faults are those with the trends parallel to the Jiaojia Fault, i.e. NNE–SSW.

Considering the above ages for the ST1 and ST2 and the age of the lamprophyre dikes, we can conclude that the formation of the dikes and veins in the Sizhuang gold deposit occurred while a change from the stress regime ST1 to ST2 was in progress. Moreover, the geometric properties of the lamprophyre dikes and quartz veins provide details about the change from ST1 to ST2 and verify the transtension tectonics during this change.

The fuzzy clustering technique of Yamaji & Sato (2011) suggests two stress states for describing the formation of the lamprophyre dikes and two stress states for describing the formation of the quartz veins. These stress states have been grouped into three regimes A, B and C (Table 1).

As mentioned above, the strike distribution of the lamprophyre dikes peaks at NNW-trending and, to a lesser degree, along the NNE trend, suggesting abrupt changes in the trend of σ_3 (*c.* 50° flip). Furthermore, all the dikes have narrow thicknesses, with none wider than 1 m, and no multiple dyke injections were observed. Therefore, it is logical to state that the resulting stress regimes A and B imply unstable stress conditions for the formation of the lamprophyre dikes (Table 1). In contrast, the distribution of the poles to the quartz veins shows the dominance of NNE trending (Figs 7d and 9b), and the banded veins with sub-parallel bands of large thicknesses (up to 5 m) were commonly observed, reflecting rather stable stress conditions. Although the stress regimes B and C for the quartz veins indicate changes in the local stresses with time, the direction of extension (σ_3) is always constant during quartz vein emplacement (Table 1).

Extension and strike-slip tectonics, i.e. transtension and associated pre-existing structures, affect the emplacement of the lamprophyre dikes and quartz veins. In particular, the NNW–SSE-trending and the subsidiary WNW–ESE-trending lamprophyre dikes intruded into the pre-existing fractures interpreted herein as subsidiary *R* and *R'* Riedel shears related to a left-lateral strike-slip deformation along the main faults like the TLF during Late Jurassic times under a NW–SE or N–S compression (or transpression) (Zhu *et al.* 2010). Under this strike-slip deformation, the Jiaojia Fault, which dips with intermediate dip angles, can be seen as a flower structure, off-strike and to the east of the TLF. In particular, stress regime A, i.e. LDA, is interpreted to represent the stress conditions in the initial stages when the NNW–SSE-trending lamprophyre dikes intruded into a large number

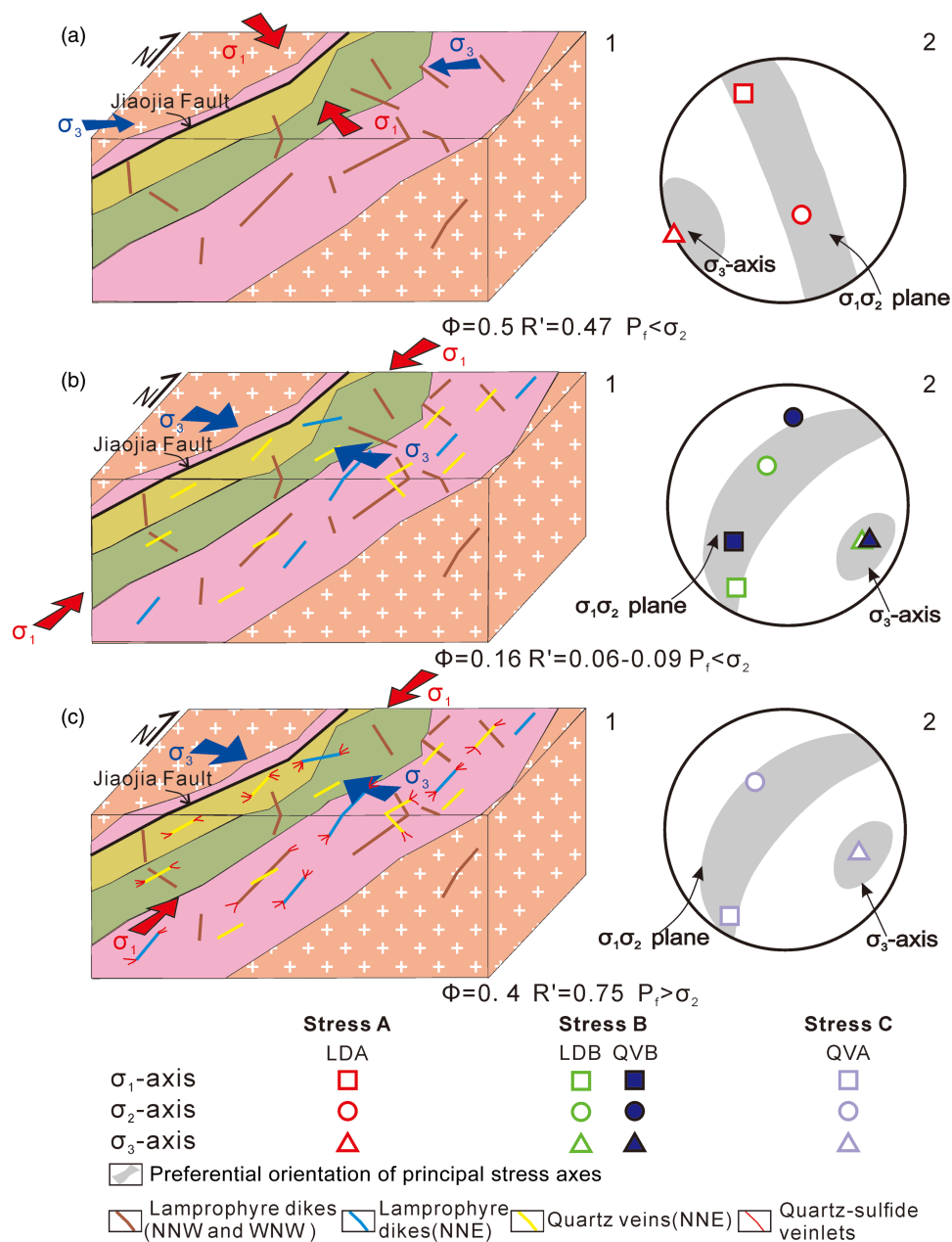


Fig. 14. (Colour online) Schematic cartoons (not to scale) showing the stress regime corresponding to lamprophyre dikes and quartz veins in the Sizhuang gold deposit. (a) E-W extension led to the development of the NNW-SSE-trending and subsidiary WNW-ESE-trending lamprophyre dikes. (b) WNW-ESE extension led to the development of the NNE-SSW-trending lamprophyre dikes and quartz veins at low P_f . (c) WNW-ESE extension led to the formation of quartz veins with a wide range of orientations in the tips of the NNE-SSW-trending dikes and the NNE-SSW quartz veins at high P_f .

of inherited structures (Fig. 14a). Dikes' intrusion, at least at the initial stages, was characterized by P_f relatively high in magnitude values, almost equal to σ_2 (Fig. 10b, c). The formation of the main bodies of the NNE-SSW-trending lamprophyre dikes and quartz veins has been dominated by WNW-ESE extension, i.e. stress regime B (i.e. LDB and QVB) (Fig. 14b). Under this stress regime, P_f was very low and smaller in magnitude than σ_2 , giving rise to the emplacement of the dikes and veins into the structures oriented mainly normal to the σ_3 axis since the fractures' permeability was poor, with only the structures that trend as the Jiaojia Fault facilitating it. Because of this, the quartz veins cross-cut the NNW-SSE-trending dikes driven by the stress regime A. However,

the girdle-type distribution of the quartz vein poles implies that their formation should include the stage dominated by the increase in fluid pressure, i.e. stress regime C (QVA). Under such conditions, the smaller pre-existing structures with a wide range of orientations can dilate, giving rise to the local geometric complexities mainly in the tips of the NNE-SSW-trending dikes and veins (Fig. 14c).

Thus, the cross-cutting network of quartz veins and fractures and the dominance of NNE-SSW-oriented quartz veins in the Sizhuang gold deposit are attributed to P_f fluctuations between $P_f > \sigma_2$ and $P_f < \sigma_2$ leading to the local stress perturbations from the regional far stress field, which remains transtension with the

σ_3 axis changing from E–W through WNW–ESE to NW–SE trend, as shown by the fault-slip analysis and their stress inversion with the TRM.

Conclusively, the lamprophyre dikes and quartz veins show a change in extension from an E–W through WNW–ESE to NW–SE trend (Fig. 14). This change reflects a significant clockwise rotation in the palaeo-Pacific plate subduction direction, and the switching time was precisely dated by the lamprophyre dating at c. 119 Ma.

7. Conclusions

The lamprophyre dikes and quartz veins in the Sizhuang gold deposit situated in the Jiaodong Peninsula in China have been studied in detail to define the accurate age and the stress regimes of their emplacement. For this purpose, the phlogopite ^{40}Ar – ^{39}Ar dating method and the fuzzy clustering technique of Yamaji & Sato (2011) are used. The dikes in their majority were dilational, trending mainly NNW–SSE and NNE–SSW with subsidiary WNW–ESE. The age of the NNE–SSW dike emplacement, which followed the inherited structures from a possible Late Jurassic strike-slip tectonics along the TLF, was at c. 119 Ma. The palaeo-stress reconstruction of the available fault-slip data provided by B Zhang et al. (2020) in the broader region of the Sizhuang gold deposit with the stress inversion TRM (Tranos, 2015) defines an E–W pure extension – transtension (ST1), and a NW–SE transtension (ST2). These stress regimes verify the stress A (E–W extension during 135–121 Ma) and stress B (NW–SE extension between 120 and 93 Ma) defined by B Zhang et al. (2020). More importantly, based on their type, i.e. pure extension – transtension (ST1) and transtension (ST2), we suggest a progressive shift in the direction of the least principal stress axis (σ_3) from E–W to NW–SE and the increased strike-slip against dip-slip kinematics along the faults.

The palaeostress analysis of the dikes indicates that the shift from the E–W to NW–SE extension gave rise to the unstable stress conditions related to the intrusion of the dikes in the Sizhuang gold deposit, which is characterized by generally low P_f values. On the other hand, the quartz veins formed under relatively stable stress conditions, showing that their formation occurred while the shift in direction of the σ_3 axis ended.

In contrast, the emplacement of the larger to smaller quartz veins is characterized by the significant P_f fluctuations and the progressive increase of the P_f . As a result, we can argue that the normal stress along the faults decreases, facilitating the strike-slip more than the dip-slip kinematics along them. The change from the ST1 to the ST2 stress regime reflects the significant clockwise rotation in the palaeo-Pacific plate subduction direction and defines the switching time at c. 119 Ma as precisely obtained by the lamprophyre dating.

Acknowledgements. We want to thank C. Pascal and an anonymous reviewer for their useful revisions and the editor O. Lacombe for his constructive comments, which greatly improved the manuscript. We thank Professor Yusheng Zhai from the China University of Geosciences (Beijing) for his help in substantially improving the manuscript. This study was financially supported by the National Natural Science Foundation of China (Grant No. 41772061).

Conflict of interest. All the authors listed declare that the material is not of any third-party copyrighted, and there are no personal relationships or competing financial interests that could have appeared to influence the work reported in this paper.

References

- Anderson EM (1939) The dynamics of sheet intrusion. *Proceedings of the Royal Society of Edinburgh* **58**, 242–51.
- André A-S, Sausse J and Lespinasse M (2001) New approach for the quantification of paleostress magnitudes: application to the Soutz vein system (Rhine graben, France). *Tectonophysics* **336**, 215–31.
- Angelier J (1975) Sur l'analyse de mesures recueillies dans des sites failés: l'utilité d'une confrontation entre les méthodes dynamique et cinématique. *Comptes Rendus de l'Académie des Sciences* **281**, 1805–8.
- Babiker M and Gudmundsson A (2004) Geometry, structure and emplacement of mafic dikes in the Red Sea Hills, Sudan. *Journal of African Earth Sciences* **38**, 279–92.
- Baer G (1991) Mechanisms of dike propagation in layered rocks and in massive, porous sedimentary rocks. *Journal of Geophysical Research* **96**, 911–29.
- Baer G, Beyth M and Reches Z (1994) Dikes emplaced into fractured basement, Timna igneous complex, Israel. *Journal of Geophysical Research Solid Earth* **99**, 24039–50.
- Bhatt S, Rana V, Lahiri S and Mamtani MA (2019) Pegmatite dike emplacement and the state of stress during cratonization: an example from the Dharwar Craton (South India). *Journal of Structural Geology* **123**, 67–80.
- Bi SJ and Zhao X (2017) ^{40}Ar – ^{39}Ar dating of the Jiehe gold deposit in the Jiaodong Peninsula, eastern North China Craton: implications for regional gold metallogeny. *Ore Geology Review* **86**, 639–51.
- Bingham C (1974) An antipodally symmetric distribution on the sphere. *Annals of Statistics* **2**, 1201–25.
- Bishop AW (1966) The strength of soils as engineering materials. *Géotechnique*, **16**, 91–130.
- Charles N, Augier R, Gumiaux C, Monie P, Chen Y, Faure M and Zhu RX (2013) Timing, duration, and role of magmatism in wide rift systems: insights from the Jiaodong Peninsula (China, East Asia). *Gondwana Research* **24**, 412–28.
- Chesley JT, Rudnick RL and Lee CT (1999) Re-Os systematics of mantle xenoliths from the East African Rift: age, structure, and history of the Tanzanian craton. *Geochimica et Cosmochimica Acta* **63**, 1203–17.
- Cong BL (1996) *Ultrahigh-pressure Metamorphic Rocks in the Dabieshan-Sulu Region of China*. Beijing: Science Press, 224 pp (in Chinese).
- Creixell C, Parada MÁ, Morata D, Vázquez P, Arce CPD and Arriagada C (2011) Middle-late Jurassic to early Cretaceous transtension and transpression during arc building in Central Chile: evidence from mafic dike swarms. *Andean Geology* **38**, 37–63.
- Dallmeyer RD and Lecorche JP (1990) $^{40}\text{Ar}/^{39}\text{Ar}$ polyorogenic mineral age record in the northern Mauritanide orogen, West Africa. *Tectonophysics* **177**, 81–107.
- Delaney PT, Pollard DD, Ziony JI and McKee EH (1986) Field relations between dikes and joints: emplacement processes and paleostress analysis. *Journal of Structural Geology* **91**, 4920–38.
- Dong Y, Genser J, Naebauer F, Zhang G, Liu X, Yang Z and Heberer B (2011) U-Pb and $^{40}\text{Ar}/^{39}\text{Ar}$ geochronological constraints on the exhumation history of the North Qingling terrane, China. *Gondwana Research* **19**, 881–93.
- Faure M, Lin W and Breton NL (2001) Where is the North China–South China boundary in eastern China? *Geology* **29**, 119–22.
- Faye GD, Yamaji A, Yonezu K, Tindell T and Watanabe K (2018) Paleostress and fluid-pressure regimes inferred from the orientations of Hishikari low sulfidation epithermal gold veins in southern Japan. *Journal of Structural Geology* **110**, 131–41.
- Goldfarb RJ, Taylor RD, Collins GS, Goryachev NA and Orlandini OF (2014) Phanerozoic continental growth and gold metallogeny of Asia. *Gondwana Research* **25**, 48–102.
- Goswami S, Lahiri S and Mamtani MA (2021) Paleostress variation during the same regional deformation in the Eastern Dharwar Craton (southern India). *Journal of Structural Geology* **143**, 104268.
- Gudmundsson A and Marinoni LB (2002) Geometry, emplacement, and arrest of dikes. *Annales Tectonicae* **13**, 71–92.
- Guo P, Santosh M and Li SR (2013) Geodynamics of gold metallogeny in the Shandong Province, NE China: an integrated geological, geophysical and geochemical perspective. *Gondwana Research* **24**, 1172–202.

- Hou ML, Jiang YH, Jiang SY, Ling HF and Zhao KD (2007) Contrasting origins of late Mesozoic adakitic granitoids from the northwestern Jiaodong Peninsula, East China: implications for crustal thickening to delamination. *Geological Magazine* **144**, 619–31.
- Jaques L and Pascal C (2017) Full paleostress tensor reconstruction using quartz veins of Panasqueira Mine, central Portugal; part I: paleopressure determination. *Journal of Structural Geology* **102**, 58–74.
- Jolly RJH and Sanderson DJ (1997) A Mohr circle construction for the opening of a pre-existing fracture. *Journal of Structural Geology* **19**, 887–92.
- Khodayar M and Einarsson P (2002) Strike-slip faulting, normal faulting, and lateral dike injections along a single fault: field example of the Glfufura fault near a Tertiary oblique rift-transform zone, Borgarfjörur, west Iceland. *Journal of Geophysical Research* **107**, 2103.
- Lahiri S and Mamtani MA (2016) Scaling the 3-D Mohr circle and quantification of paleostress during fluid pressure fluctuation: application to understand gold mineralization in quartz veins of Gadag (southern India). *Journal of Structural Geology* **88**, 63–72.
- Lahiri S, Rana V, Bhatt S and Mamtani MA (2020) Paleostress and statistical analysis using quartz veins from mineralized and non-mineralized zones: application for exploration targeting. *Journal of Structural Geology* **133**, 104006. doi: 10.1029/2001JB000150.
- Lee JY, Marti K, Severinghaus JP, Kawamura K, Yoo HS, Lee JB and Kim JS (2006) A redetermination of the isotopic abundances of atmospheric Ar. *Geochimica et Cosmochimica Acta* **70**, 4507–12.
- Li JW, Bi SJ, Selby D, Chen L, Vasconcelos P, Thiede D, Zhou MF, Zhao XF, Li ZK and Qiu HN (2012) Giant Mesozoic gold provinces related to the destruction of the North China craton. *Earth and Planetary Science Letters* **349–350**, 26–37.
- Li JW, Vasconcelos PM, Zhou MF, Zhao XF and Ma CQ (2006) Geochronology of the Pengjiakuang and Rushan gold deposits, eastern Jiaodong gold province, northeastern China: implications for regional mineralization and geodynamic setting. *Economic Geology* **101**, 1023–38.
- Li L, Li SR, Santosh M, Li Q, Gu Y, Lü WJ, Zhang HF, Shen JF and Zhao GC (2016) Dike swarms and their role in the genesis of world-class gold deposits: insights from the Jiaodong peninsula, China. *Journal of Asian Earth Sciences* **130**, 2–22.
- Li S, Xiao Y, Liu D, Chen Y, Ge N, Zhang Z, Sun S, Cong B, Zhang R, Hart SR and Wang S (1993) Collision of the North China and Yangtze blocks and formation of coesite-bearing eclogites: timing and processes. *Chemical Geology* **109**, 89–111.
- Liu JG, Rudnick RL, Walker RJ, Xu WL, Gao S and Wu FY (2015) Big insights from tiny peridotites: evidence for persistence of Precambrian lithosphere beneath the eastern North China Craton. *Tectonophysics* **650**, 104–12.
- Liu JL, Ji M, Ni JL, Shen L, Zheng YY, Chen XY and Craddock JP (2021) Inhomogeneous thinning of a cratonic lithospheric keel by tectonic extension: the Early Cretaceous Jiaodong Peninsula-Liaodong Peninsula extensional provinces, eastern North China craton. *Geological Society of America Bulletin* **133**, 159–76.
- Liu SF, Gurnis M, Ma PF and Zhang B (2017) Reconstruction of northeast Asian deformation integrated with western Pacific plate subduction since 200 Ma. *Earth-Science Reviews* **175**, 114–42.
- Lu HZ, Archambault G, Li Y and Wei J (2007) Structural geochemistry of gold mineralization in the Linglong-Jiaojia district, Shandong Province, China. *Chinese Journal of Geochemistry* **26**, 215–34 (in Chinese with English abstract).
- Martínez-Poza AI and Druguet E (2016) Structure and tectonic setting of the SE Sardinia mafic dike swarm: insights for the stress state during magma emplacement in the upper crust. *Journal of Geodynamics* **101**, 170–85.
- Martínez-Poza AI, Druguet E, Castaño LM and Carreras J (2014) Dike intrusion into a pre-existing joint network: the Aiguablava lamprophyre dike swarm (Catalan Coastal Ranges). *Tectonophysics* **1263**, 1–16.
- Matchan EL and Phillips D (2014) High precision multi-collector $^{40}\text{Ar}/^{39}\text{Ar}$ dating of young basalts: Mount Rouse volcano (SE Australia) revisited. *Quaternary Geochronology* **22**, 57–64.
- Mazzarini F and Isola I (2007) Hydraulic connection and fluid overpressure in upper crustal rocks: evidence from the geometry and spatial distribution of veins at Botrona quarry, southern Tuscany, Italy. *Journal of Structural Geology* **29**, 1386–99.
- Mazzarini F, Isola I, Ruggieri G and Boschi C (2010) Fluid circulation in the upper brittle crust: thickness distribution, hydraulic transmissivity fluid inclusion and isotopic data of veins hosted in the Oligocene sandstones of the Macigno Formation in southern Tuscany, Italy. *Tectonophysics* **493**, 118–38.
- Mazzarini F and Musumeci G (2008) Hydrofracturing-related sill and dike emplacement at shallow crustal levels: the Eastern Elba Dike Complex, Italy. In *Structure and Emplacement of High-Level Magmatic Systems* (ed. K. Thomson), pp. 121–9. *Geological Society of London, Special Publication no. 302*.
- McKeagney CJ, Boulter CA, Jolly RJH and Foster RP (2004) 3-D Mohr circle analysis of vein opening, Indarama lode-gold deposit, Zimbabwe: implications for exploration. *Journal of Structural Geology* **26**, 1275–91.
- Meng QR (2003) What drove late Mesozoic extension of the northern China-Mongolia tract? *Tectonophysics* **369**, 155–74.
- Mondal TK and Mamtani MA (2013) 3-D Mohr circle construction using vein orientation data from Gadag (southern India): implications to recognize fluid pressure fluctuation. *Journal of Structural Geology* **56**, 45–56.
- Ni JL, Liu JL, Tang XL, Yang HB, Xia ZM and Zhang TT (2016) Early Cretaceous exhumation of the Sulu orogenic belt as a consequence of the eastern Eurasian tectonic extension: insights from the newly discovered Wulian metamorphic core complex, eastern China. *Journal of the Geological Society* **173**, 531–49.
- Pascal C (2021) *Paleostress Inversion Techniques: Methods and Applications for Tectonics*. Amsterdam: Elsevier, 274 pp.
- Pascal C, Jaques L and Yamaji A (2022) Full paleostress tensor reconstruction using quartz veins of Panasqueira Mine, central Portugal, part II: Final results. *Journal of Structural Geology* **162**, 104688.
- Phillips D, Matchan EL, Honda M and Kuiper KF (2017) Astronomical calibration of $^{40}\text{Ar}/^{39}\text{Ar}$ reference minerals using high-precision, multi-collector (ARGUSVI) mass spectrometry. *Geochimica et Cosmochimica Acta* **196**, 351–69.
- Pollard DD (1987) Elementary fracture mechanics applied to the structural interpretation of dikes. In *Mafic Dike Swarms* (eds HC Halls and WF Fahrig), pp. 5–24. St John's: *Geological Association of Canada, Special Paper no. 34*.
- Pollard DD, Muller OH and Dockstader DR (1975) The form and growth of fingered sheet intrusions. *Geological Society of America Bulletin* **86**, 351–63.
- Ratschbacher L, Hacker BR, Webb LE, McWilliams M, Ireland T, Dong SW, Calvert A, Chateigner D and Wenk HR (2000) Exhumation of the ultra-high-pressure continental crust in east central China: Cretaceous and Cenozoic unroofing and the Tan-Lu fault. *Journal of Geophysical Research* **105**, 13,303–38.
- Ren FL, Zhang YQ, Qiu LG, Liu ZQ and Wang DH (2007) Evolution of the structural stress field in Jiaolai basin in Cretaceous. *Geotectonica et Metallogenia* **31**, 157–67 (in Chinese with English abstract).
- Sager WW (2006) Cretaceous paleomagnetic apparent polar wander path for the Pacific Plate calculated from Deep Sea Drilling Project and Ocean Drilling Program basalt cores. *Physics of the Earth and Planetary Interiors* **156**, 329–49.
- Santosh M, Wilde SA and Li JH (2007) Timing of Paleoproterozoic ultrahigh temperature metamorphism in the North China Craton: evidence from SHRIMP U-Pb zircon geochronology. *Precambrian Research* **159**, 178–96.
- Sato K, Yamaji A and Tonai S (2013) Parametric and non-parametric statistical approaches to the determination of paleostress from dilatant fractures: application to an Early Miocene dike swarm in central Japan. *Tectonophysics* **588**, 69–81.
- Skarmeta J (2011) Interaction between magmatic and tectonic stresses during dike intrusion. *Andean Geology* **38**, 393–413.
- Steiger RH and Jager E (1977) Subcommittee on Geochronology: Convention on the Use of Decay Constants in Geo- and Cosmochronology. *Earth and Planetary Science Letters* **36**, 359–62.
- Sun WD, Ding X, Hu YH and Li XH (2007) The golden transformation of the Cretaceous plate subduction in the west Pacific. *Earth and Planetary Science Letters* **262**, 533–42.
- Tang J, Zheng YF, Wu YB, Gong B and Liu XM (2007) Geochronology and geochemistry of metamorphic rocks in the Jiaobei terrane: constraints on its tectonic affinity in the Sulu orogen. *Precambrian Research* **152**, 48–82.

- Tran NH and Ravoof A** (2007) Coupled fluid flow through discrete fracture network: a novel approach. *International Journal of Applied Mathematics and Computer Science* **1**, 295–9.
- Tranos MD** (2015) TR method (TRM): a separation and stress inversion method for heterogeneous fault-slip data driven by Andersonian extensional and compressional stress regimes. *Journal of Structural Geology* **79**, 57–74.
- Tranos MD** (2017) The use of Stress Tensor Discriminator Faults in separating heterogeneous fault-slip data with best-fit stress inversion methods. *Journal of Structural Geology* **102**, 168–78.
- Tranos MD, Kachev VN and Mountrakis DM** (2008) Transtensional origin of the NE–SW Simitli basin along the Strouma (Strymon) Lineament, SW Bulgaria. *Journal of the Geological Society* **165**, 499–510.
- Wang J, Chang SC, Chen Y and Yan SY** (2019) Early Cretaceous transpressional and transtensional tectonics straddling the Sulu orogenic belt, East China. *Geoscience Frontiers* **10**, 2287–300.
- Wang J, Chang SC, Lin PJ, Lu HB, Zhu XQ, Fu YT and Zhang HC** (2016) Evidence of Early Cretaceous transpression in the Sulu orogenic belt, eastern China. *Tectonophysics* **687**, 44–55.
- Wang T, Zheng Y, Zhang J, Zeng L, Donskaya T, Guo L and Li J** (2011) Pattern and kinematic polarity of late Mesozoic extension in continental NE Asia: perspectives from metamorphic core complexes. *Tectonics* **30**, TC6007.
- Wang ZL, Yang LQ, Deng J, Santosh M, Zhang HF, Liu Y, Li RH, Huang T, Zheng XL and Zhao H** (2014) Gold-hosting high Ba–Sr granitoids in the Xincheng gold deposit, Jiaodong Peninsula, East China: petrogenesis, tectonic setting. *Journal of Asian Earth Sciences* **95**, 274–99.
- Wang ZL, Yang LQ, Guo LN, Marsh E, Wang JP, Liu Y, Zhang C, Li RH, Zhang L, Zheng XL and Zhao RX** (2015) Fluid immiscibility and gold deposition in the Xincheng deposit, Jiaodong Peninsula, China: a fluid inclusion study. *Ore Geology Review* **65**, 701–17.
- Wei YJ, Yang LQ, Feng JQ, Wang H, Lv GY, Li WC and Liu SG** (2019) Ore-fluid evolution of the Sizhuang orogenic gold deposit, Jiaodong Peninsula, China. *Minerals* **9**, 1–20.
- Xiao WJ, Windley BF, Hao J and Zhai MG** (2003) Accretion leading to collision and the Permian Solonker suture, Inner Mongolia, China: termination of the central Asian orogenic belt. *Tectonics* **22**, 1069.
- Yamaji A** (2016) Genetic algorithm for fitting a mixed Bingham distribution to 3D orientations: a tool for the statistical and paleostress analyses of fracture orientations. *Island Arc* **25**, 72–83.
- Yamaji A and Sato K** (2011) Clustering of fracture orientations using a mixed Bingham distribution and its application to paleostress analysis from dike or vein orientations. *Journal of Structural Geology* **33**, 1148–57.
- Yamaji A, Sato K and Tonai S** (2010) Stochastic modeling for the stress inversion of vein orientations: paleostress analysis of Pliocene epithermal veins in southwestern Kyushu, Japan. *Journal of Structural Geology* **32**, 1137–46.
- Yan LJ, Zhu G, Lin SZ and Zhao T** (2014) Neotectonic activity and formation mechanism of the Yishu Fault Zone. *Science China – Earth Sciences* **57**, 614–29.
- Yang JH, Chung SL, Wilde SA, Wu FY, Chu MF, Lo CH and Fan HR** (2005) Petrogenesis of post-orogenic syenites in the Sulu orogenic belt, East China: geochronological, geochemical and Nd–Sr isotopic evidence. *Chemical Geology* **214**, 99–125.
- Yang KF, Fan HR, Santosh M, Hu FF, Wilde SA, Lan TG, Lu LN and Liu YS** (2012) Reactivation of the Archean lower crust: implications for zircon geochronology, elemental and Sr–Nd–Hf isotopic geochemistry of late Mesozoic granitoids from northwestern Jiaodong terrane, the North China craton. *Lithos* **146**, 112–27.
- Yang KF, Jiang P, Fan HR, Zuo YB and Yang YH** (2018) Tectonic transition from a compressional to extensional metallogenic environment at ~120 Ma revealed in the Hushan gold deposit, Jiaodong, North China craton. *Journal of Asian Earth Sciences* **160**, 408–25.
- Yang LQ, Deng J, Goldfarb RJ, Zhang J, Gao BF and Wang ZL** (2014) $^{40}\text{Ar}/^{39}\text{Ar}$ geochronological constraints on the formation of the Dayingezhuang gold deposit: new implications for timing and duration of hydrothermal activity in the Jiaodong gold province, China. *Gondwana Research* **25**, 1469–83.
- Yang LQ, Dilek Y, Wang ZL, Weinberg RF and Liu Y** (2018) Late Jurassic, high Ba–Sr Linglong granites in the Jiaodong Peninsula, east China: lower crustal melting products in the eastern North China craton. *Geological Magazine* **55**, 1040–62.
- Yang QY, Santosh M, Shen JF and Li SR** (2014) Juvenile vs. recycled crust in NE China: zircon U–Pb geochronology, Hf isotope and an integrated model for Mesozoic gold mineralization in the Jiaodong Peninsula. *Gondwana Research* **25**, 1445–68.
- York D** (1969) Least squares fitting of a straight line with correlated errors. *Earth and Planetary Science Letters* **5**, 320–4.
- Zhang B, Liu SF, Lin CF, Shen WJ and Li XY** (2020) Reconstruction of the stress regime in the Jiaolai Basin, East Asian margin, as decoded from fault-slip analysis. *Journal of Structural Geology* **141**, 104190.
- Zhang L, Weinberg RF, Yang LQ, Groves DI, Sai SX, Matchan E, Phillips D, Kohn BP, Miggins DP, Liu Y and Deng J** (2020) Mesozoic orogenic gold mineralization in the Jiaodong Peninsula, China: a focused event at 120 ± 2 Ma during cooling of pregold granite intrusions. *Economic Geology* **115**, 415–41.
- Zhang YQ, Dong SW and Shi W** (2003) Cretaceous deformation history of the middle Tan–Lu fault zone in Shandong Province, eastern China. *Tectonophysics* **363**, 243–58.
- Zhang YQ, Li JL, Zhang T, Dong SW and Yuan JY** (2008) Cretaceous to Paleocene tectonosedimentary evolution of the Jiaolai basin and the contiguous areas of the Shandong Peninsula (North China) and its geodynamic implications. *Acta Geologica Sinica* **82**, 1229–57.
- Zhang YQ, Li JL, Zhang T & Yuan JY** (2007) Late Mesozoic kinematic history of the Mouping–Jimo fault zone in Jiaodong peninsula, Shandong Province, East China. *Geological Review* **53**, 289–300 (in Chinese with English abstract).
- Zhao GC, Sun M, Wilde SA and Li SZ** (2005) Late Archean to Paleoproterozoic evolution of the North China Craton: key issues revisited. *Precambrian Research* **136**, 177–202.
- Zhu G, Niu ML, Xie CL and Wang YS** (2010) Sinistral to normal faulting along the Tan–Lu Fault Zone: evidence for geodynamic switching of the East China continental margin. *Journal of Geology* **118**, 277–93.
- Zhu G, Wang YS, Liu GS, Niu ML, Xie CL and Li CC** (2005) $^{40}\text{Ar}/^{39}\text{Ar}$ dating of strike-slip motion on the Tan–Lu Fault Zone, East China. *Journal of Structural Geology* **27**, 1379–98.
- Zhu RX, Fan HR, Li JW, Meng QR and Li SR** (2015) Decratonic gold deposits. *Chinese Science: Geoscience* **58**, 1523–37.
- Zhu RX and Xu YG** (2019) The subduction of the west Pacific plate and the destruction of the North China Craton. *Science China – Earth Sciences* **62**, 1340–50.